Evaluation of hydrodynamic coefficients and sensitivity analysis of a work-class ROV by planar motion mechanism tests

Ruinan Guo[1], Yingfei Zan[*1], Xiaofang Luo[2], Xiandong Ma[3], Tiaojian Xu, Duanfeng Han[1], Dejun Li, Xu Bai[4]

[1] College of Shipbuilding Engineering, Harbin Engineering University, Harbin 150001, China
[2] School of Economics and Management, Jiangsu University of Science and Technology, Zhenjiang 212003, China
[3] School of Engineering, Lancaster University, Lancaster, UK
[4] School of Naval Architecture & Ocean Engineering, Jiangsu University of Science and Technology, Zhenjiang 212003, China
* Corresponding author: zanyingfei@hrbeu.edu.cn (Yingfei Zan)

Abstract

The paper presents the analysis of the hydrodynamic forces and moments concerning the drag and PMM model experiments which aims to model and simplify the maneuverability mathematical model for a work-class ROV. The experiments performed in the nonlinear wave channel of the Dalian University of Technology included static drag tests, static drift and trim drag tests, surge, pure sway, pure heave, pure roll, pure pitch, and pure yaw tests. The viscous hydrodynamic coefficients in a quadratic absolute value function and all the inertial hydrodynamic coefficients were estimated. The results of hydrodynamic load and coefficients showed significant nonlinear and asymmetrical characteristics. The Normalized Sensitivity Coefficient (NSC) was carried out to investigate the sensitivity of both the viscous and inertial hydrodynamic coefficients considering the multi-DOF motion and velocity effect. The drag, drift, and stationary random motions were defined to examine the sensitivity. The comparison of the motion simulation results of simplified and complete models showed that the threshold value of 0.01 for NSC to filter the coefficients is suitable for the ROV.

Keywords: PMM, ROV, maneuverability, hydrodynamic coefficients, sensitivity analysis, Normalized Sensitivity Coefficient, mathematical model simplify.

1. Introduction

1.1 Background

Underwater vehicles provide a unique technical solution to address the challenges involved in the support of offshore marine renewable technology operations. Recently, the increasing speed capability and positional accuracy of Remotely Operated Vehicles (ROVs) allowed them to operate in the highest currents experienced in the shallow waters of marine renewable technologies [1]. ROVs are widely used for the installation, damage detection, and biodiversity studies of the offshore wind power industry. The rigging connecting the structure and the vessel was checked by using an ROV in the monopile installation of the offshore wind turbine structure[2]. The hook can be removed and the belt around the buoy can be opened by the ROV in the dynamic installation of anchors for floating offshore wind turbines [3]. Preventive maintenance on cables for offshore floating wind turbines in a life cycle perspective is performed with an anchor handling towing supply vessel that features diving support and ROV [4, 5]. Deploymenting an ROV is a long-term approach for remote monitoring and inspection of distributed assets within the offshore Marine Renewable Energy farm [6]. A top-tension-meter and a series of bi-axial inclinometers along the line can do real-time riser or mooring monitoring powered by ROV-replaceable battery packs for the structural health monitoring of TLP-FOWT [7]. An ROV was used to collect the data on species communities to investigate the contribution of offshore wind farms to epibenthic biodiversity in the southern North Sea [8].

However, the applications of ROVs for damage detection are limited because of the high operation cost and safety considerations. The demand for ROVs is growing with the increase in the number of OWTs and other marine structures [9]. The motion of the floating wind turbine platform has a significant impact on control systems for automated visual inspection and intervention using ROV manipulators [10]. One of the challenges of ROV subsea operations near wind turbine sites is the strong currents, high waves, and the need to operate near underwater structures that require a very precise control system. A precise control system is essential to keep the ROV stable and prevent a situation in which the ROV pilot struggles to fight against the current to proceed with the operation [11]. An important consideration for an ROV operation is maneuverability, especially influenced by the multi-degree of freedom (DOF) motion and the umbilical cable tension due to the surface vessel motion in waves. Precise modeling of hydrodynamic load on ROV is necessary to ensure the success rate of subsea operations and to comply with safety requirements.

1.2 PMM tests for underwater vehicles

A maneuvering model with compact notation using matrices and vectors is commonly used in motion simulations and control systems design. Fossen presented a 6-DOF model for AUVs and ROVs [12]. Scholars have shown some interest in the asymmetric and high-order hydrodynamic model of ROV[13-15]. A crucial piece of equipment used to perform captive model tests in the towing tank or water channel is the Planar Motion Mechanism (PMM) and the data is used to estimate the hydrodynamic derivatives after maneuvering tests[16]. The reason why the PMM has been widely used in the last decades is the advantage relies on its reasonable accuracy in obtaining both damping and added mass derivatives. The purpose of the PMM tests is that apply forced harmonic motion to observe the dynamic hydrodynamic of an underwater vehicle. The vertical PMM could be achieved by two slider-crank mechanisms one link on the stem and the other linked in the stern of the test model. By superposition of various DOFs of motion, the PMM tests can measure all the hydrodynamic coefficients of the mathematical model. The added mass and inertia can be acquired from the pure heaving motion and pure pitching motion respectively in a set of vertical PMM tests[17]. Jung and Jeong et al measured the vertical damping and inertial hydrodynamic coefficients of an underwater glider in connection with vertical linear velocity and pitching angular velocity [18]. Jun et al investigated the water depth effect on the submarine with different motion periods via vertical PMM tests [19, 20]. A water tunnel using vertical PMM that changes the frequencies of pure pitch and heave motions by a voltage change in the three-phase motor and different amplitudes can be attained as a result of slider motion in the grooved crank. The static and dynamic tests were conducted to estimate the underwater vehicle hydrodynamic derivatives using the above PMM [21]. Park et al set the AUV model at the self-propulsion point and measured the forces on the body and control fins with vertical PMM equipment to establish a mathematical maneuvering model using a whole vehicle model[22]. Xu et al calculated inertial coefficients and discussed the properties of the cross-inertial coefficients, which are related to the inertial forces and moments induced by the motion in other directions [13].

The horizontal PMM could be constructed by a threaded spindle and a vertical machine. The same as vertical PMM, the PMM decouples the vertical and horizontal motion, therefore horizontal planar motion tests of an underwater vehicle should be performed by rotating the model by 90° about the propeller shaft axis[23]. The mounting modes of underwater vehicles can be divided into yaw, pitch, and roll modes according to the relative location of the hull and the strut of a horizontal PMM [24]. By this means, coupling with a flexible installation method of an underwater vehicle, all six DOF hydrodynamic derivatives can be estimated [25]. The PMM procedure, which includes sway and yaw oscillations in addition to the forward motion, determines the coefficients that are correlated to the transverse force, yaw moment, and lateral and turning velocities[26]. Lee et al estimated the hydrodynamic maneuvering derivatives of heave-pitch coupling motion for a Ray-type Underwater Glider with a horizontal PMM test[27]. It is possible to study the hydrodynamics of underwater vehicles in large drift and trim angles accompanied by horizontal PMM [28]. Liang et al carried out a set of oblique towing tests containing high attack angles, pure heave tests, and pure pitch tests, which bring about a low-order and piecewise mathematical model of a submarine [29]. Besides the slider-crank mechanism and threaded spindle-vertical machine mechanism, the six DOF motion platform was also adopted as PMM. Profit from the multi-DOF coupled motion, the efficiency of measuring the hydrodynamic coefficients of physical models of ships and offshore structures is improved by the device[30]. Xu performed a series of PMM tests via a 6-DOF hexapod motion platform for the estimation of nondimensionalized hydrodynamic coefficients of the ship by least square support vector machine. The validation process was carried out to test the performance and accuracy of the resulting nonlinear maneuvering models [31, 32].

1.3 Sensitivity analysis for underwater vehicles

There may be hundreds of hydrodynamic coefficients for a complete mathematical model of a work-class open-frame ROV. Too many parameters are difficult to identify without particular costly maneuvers for parameter identification and motion prediction cases. A simplified model can improve the efficiency of a model-based controller and state estimators. Therefore, it is necessary to analyze the sensitivity of the mathematical mode coefficients, to generate the ranking of the hydrodynamic coefficients and identify the coefficients that have a negligible influence on the output variability[33]. The direct method and indirect method are used for sensitivity analysis of an underwater vehicle in the field of engineering. Yeo *et al.* carried out the equation of the sensitivity matrix in the direct method by rewriting the maneuverability mathematical model of the submarine and examined the influences of hydrodynamic coefficients on the prediction of submarine maneuverability [34]. Abolvafaie *et al*. calculated the hydrodynamic coefficients' sensitivity values in the direct method by using turning circle maneuver and zigzag maneuver [35]. The overshoot maneuver and turning circle maneuver could be chosen as the response motion for a submarine in the indirect method [36]. To be specific, the radius of the turning circle could be chosen as a measure of steady-state response and the advance could be chosen as a measure of the transient response. In an overshoot maneuver, the overshoot angle and width of the path could be chosen as a measure of the straight and level flight response to study the sensitivity of underwater vehicles' response [37]. The velocity is an optional parameter to investigate the sensitivity of an underwater vehicle[38], such as overshoot of sway, yaw velocity, and yaw rate in a steady state [39]. The specific method is to vary the coefficient values by a limited percentage one at a time while other coefficients are fixed at their original values. And repeated the mathematical model-based trajectory simulations to find the most evident coefficients of an underwater vehicle [40, 41]. Wang et al compared the simulation results that were calculated from the mathematical model of which test values varying in the normal distribution diagram with the CFD results to examine the contribution of sway force, heave force, pitch and yaw moment, and the corresponding hydrodynamic coefficients [42]. Besides the hydrodynamic coefficients, the design parameters are another significant influence variate on the sensitivity of a system. By changing the length-to-diameter ratio and the location of the shaftline, the sensitivity of the added mass coefficients was obtained [43]. Jeon *et al*. the geometric parameters for the bare hull and rudder to be the hull form design parameters to calculate the total sensitivity and partial sensitivity by the chain rule to design the hull form of an underwater vehicle in the conceptual design phase [44]. In a word, one of the keys to the sensitivity analysis of underwater vehicles is the trajectory. The overshoot maneuver and turning circle maneuver of an axisymmetric body were frequently used. However, they are not the typical trajectory of the work-class ROV. And the existing standard of sensitivity analysis of submarines and AUVs is not suitable for work-class ROVs.

1.4 Objectives of this study

Therefore, this article presents a sensitivity analysis of hydrodynamic coefficients for a work-class ROV in different trajectories based on the maneuverability mathematical model obtained from PMM experiments. The contribution is that it presents a new train of thought about simplifying the mathematical model to suit the 6-DOF motion ROV in the full domain of the designed speed. A normalized coefficient was used to analyze the sensitivity of hydrodynamic coefficients which could reveal the relation between the sensitivity, the size of the coefficients, the hydrodynamic load, and the moving speed.

The paper is arranged as follows: The mathematical model is established in section 2; The test conditions and equipment are listed in section 3; section 4 reports and analyzes the hydrodynamic loads and coefficients; section 5 presents the sensitivity analysis method and results; there is a few discussion in section 6 about the findings and reasons of our investigation.

2. Mathematical model

There are two coordinate systems used in the experiment, the space-fixed coordinate system $O\text{-}x_0y_0z_0$ and the body-fixed coordinate system $G\text{-}xyz$. Both two coordinate systems are right-handed. The origin O is fixed on a point on earth and the Oz_0 axis along the gravity direction. The origin G is fixed on the gravity central of the test model. The Gx and Gy axis points to the stem and the starboard of the ROV model respectively. The surge, sway, and heave velocity (u, v, w) and the roll, pitch, and yaw angular velocity (p, q, r) are defined in the body-fixed coordinate system. The attack and drift angle (α, β) are defined according to the navigation speed V and the body-fixed coordinate system.

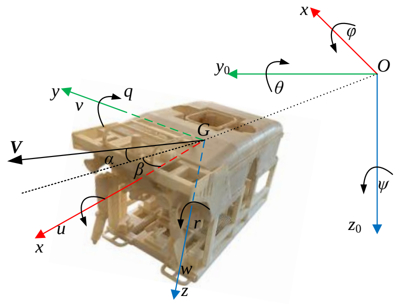

Figure 1. The space-fixed and body-fixed coordinate systems

The hydrodynamic model in the paper is based on second-order modulus functions. The approach is to describe the total hydrodynamic surge X, sway Y, heave, and Z forces and roll K, pitch M, and yaw moment N acting on an ROV as general functions of the state variables at a certain instant such as surge, sway, and heave velocities and roll, pitch, and yaw angular velocities (u, v, w, p, q, r, respectively) and accelerations ($\dot{u}$, $\dot{v}$, $\dot{w}$, $\dot{p}$, $\dot{q}$, and $\dot{r}$ respectively) in the body-fixed coordinate system. The momentum theorem derives the six degrees of freedom equations of motion in the body-fixed coordinate system as follows.

$$\begin{array}{ll} m(\dot{u}+qw-rv)=X & I_x\dot{p}+(I_z-I_y)qr=K \\ m(\dot{v}+ru-pw)=Y & I_y\dot{q}+(I_x-I_z)rp=M \\ m(\dot{w}+pv-qu)=Z & I_z\dot{r}+(I_y-I_z)pq=N \end{array} \tag{1}$$

where, m is the mass of the ROV. Ix, Iy, and Iz represent the moments of inertia of the ROV to the x, y, and z axes of the body-fixed coordinate system, respectively. The following hydrodynamic and hydrostatic mathematical model is used to represent the external forces.

$$\{X \quad Y \quad Z \quad K \quad M \quad N\}^T = \underset{\text{inertia load}}{\boldsymbol{F}_1} + \underbrace{\boldsymbol{F}_2+\boldsymbol{F}_3}_{\text{viscous load}} + \boldsymbol{F}_{\boldsymbol{g}} \tag{2}$$

where external forces include inertia, viscous loads, the submerged weight of the body, and buoyancy force $\boldsymbol{F}_{\boldsymbol{g}}$. $\boldsymbol{F}_1$ indicates the hydrodynamic force related to the added mass. $\boldsymbol{F}_2$, $\boldsymbol{F}_3$ are hydrodynamic forces that are associated with uncoupled velocity and coupled velocity in horizontal and vertical motion. In this study, the sum of added mass Coriolis and centripetal terms together with hydrodynamic damping terms is used in the model to avoid overparametrization.

The viscous hydrodynamic loads mentioned above are mainly caused by the asymmetric shape of work-class open frame ROV, the movement across degrees of freedom, and the sea current that is not the main direction of movement. The shape of the open-frame ROV is not symmetrical along the transverse section of its midships due to the influence of the carrying equipment. The asymmetric shape will make the mathematical expression of the viscous hydrodynamic of ROV appear more nonlinear terms. The hydrodynamic coefficients of the same hydrodynamic components are not equal when the ROV is moving in opposite collinear directions. To build an accurate and continuous hydrodynamic model, the mathematical hydrodynamic model needs to include the absolute value of the higher-order velocity. The mathematical model is as follows:

- Inertia loads

$$\boldsymbol{F}_1=\begin{bmatrix} 1/2\rho L^3(X'_{\dot{u}}\dot{u}+X'_{\dot{v}}\dot{v}+X'_{\dot{w}}\dot{w}+LX'_{\dot{p}}\dot{p}+LX'_{\dot{q}}\dot{q}+LX'_{\dot{r}}\dot{r}) \\ 1/2\rho L^3(Y'_{\dot{u}}\dot{u}+Y'_{\dot{v}}\dot{v}+Y'_{\dot{w}}\dot{w}+LY'_{\dot{p}}\dot{p}+LY'_{\dot{q}}\dot{q}+LY'_{\dot{r}}\dot{r}) \\ 1/2\rho L^3(Z'_{\dot{u}}\dot{u}+Z'_{\dot{v}}\dot{v}+Z'_{\dot{w}}\dot{w}+LZ'_{\dot{p}}\dot{p}+LZ'_{\dot{q}}\dot{q}+LZ'_{\dot{r}}\dot{r}) \\ 1/2\rho L^4(K'_{\dot{u}}\dot{u}+K'_{\dot{v}}\dot{v}+K'_{\dot{w}}\dot{w}+LK'_{\dot{p}}\dot{p}+LK'_{\dot{q}}\dot{q}+LK'_{\dot{r}}\dot{r}) \\ 1/2\rho L^4(M_{\dot{u}}\dot{u}+M_{\dot{v}}\dot{v}+M'_{\dot{w}}\dot{w}+LM'_{\dot{p}}\dot{p}+LM'_{\dot{q}}\dot{q}+LM'_{\dot{r}}\dot{r}) \\ 1/2\rho L^4(N'_{\dot{u}}\dot{u}+N'_{\dot{v}}\dot{v}+N'_{\dot{w}}\dot{w}+LN'_{\dot{p}}\dot{p}+LN'_{\dot{q}}\dot{q}+LN'_{\dot{r}}\dot{r}) \end{bmatrix} \tag{3}$$

- Viscous loads related to uncoupled velocities

$$\boldsymbol{F}_2=\{X_2 \quad Y_2 \quad Z_2 \quad K_2 \quad M_2 \quad N_2\}^T \tag{4}$$

where,

$$X_2 \Big/ \tfrac{1}{2}\rho L^2 = X'_{u|u|}u|u| + X'_{uu}u^2 + X'_{v|v|}v|v| + X'_{vv}v^2 + X'_{w|w|}w|w| + X'_{ww}w^2 + \sqrt{gl}(X'_{|u|}|u| + X'_u u + X'_{|v|}|v| + X'_v v + X'_{|w|}|w| + X'_w w + X'_p p + X'_q q + X'_r r)$$

$$Y_2 \Big/ \tfrac{1}{2}\rho L^2 = Y'_{u|u|}u|u| + Y'_{uu}u^2 + Y'_{v|v|}v|v| + Y'_{vv}v^2 + Y'_{w|w|}w|w| + Y'_{ww}w^2 + \sqrt{gl}(Y'_{|u|}|u| + Y'_u u + Y'_{|v|}|v| + Y'_v v + Y'_{|w|}|w| + Y'_w w + Y'_p p + Y'_q q + Y'_r r)$$

$$Z_2 \Big/ \tfrac{1}{2}\rho L^2 = Z'_{u|u|}u|u| + Z'_{uu}u^2 + Z'_{v|v|}v|v| + Z'_{vv}v^2 + Z'_{w|w|}w|w| + Z'_{ww}w^2 + \sqrt{gl}(Z'_{|u|}|u| + Z'_u u + Z'_{|v|}|v| + Z'_v v + Z'_{|w|}|w| + Z'_w w + Z'_p p + Z'_q q + Z'_r r)$$

$$K_2 \Big/ \tfrac{1}{2}\rho L^3 = K'_{u|u|}u|u| + K'_{uu}u^2 + K'_{v|v|}v|v| + K'_{vv}v^2 + K'_{w|w|}w|w| + K'_{ww}w^2 + \sqrt{gl}(K'_{|u|}|u| + K'_u u + K'_{|v|}|v| + K'_v v + K'_{|w|}|w| + K'_w w + K'_p p + K'_q q + K'_r r)$$

$$M_2 \Big/ \tfrac{1}{2}\rho L^3 = M'_{u|u|}u|u| + M'_{uu}u^2 + M'_{v|v|}v|v| + M'_{vv}v^2 + M'_{w|w|}w|w| + M'_{ww}w^2 + \sqrt{gl}(M'_{|u|}|u| + M'_u u + M'_{|v|}|v| + M'_v v + M'_{|w|}|w| + M'_w w + M'_p p + M'_q q + M'_r r)$$

$$N_2 \Big/ \tfrac{1}{2}\rho L^3 = N'_{u|u|}u|u| + N'_{uu}u^2 + N'_{v|v|}v|v| + N'_{vv}v^2 + N'_{w|w|}w|w| + N'_{ww}w^2 + \sqrt{gl}(N'_{|u|}|u| + N'_u u + N'_{|v|}|v| + N'_v v + N'_{|w|}|w| + N'_w w + N'_p p + N'_q q + N'_r r)$$

- Viscous loads related to uncoupled velocities

$$\boldsymbol{F}_3 = \{X_3 \quad Y_3 \quad Z_3 \quad K_3 \quad M_3 \quad N_3\}^T, \tag{5}$$

where,

$$\begin{aligned}
X_3 &= \frac{1}{2}\rho L^2(X'_{u|v|}u|v| + X'_{uv}uv + X'_{u|w|}u|w| + X'_{uw}uw) & K_3 &= \frac{1}{2}\rho L^3(K'_{u|v|}u|v| + K'_{uv}uv + K'_{u|w|}u|w| + K'_{uw}uw) \\
Y_3 &= \frac{1}{2}\rho L^2(Y'_{u|v|}u|v| + Y'_{uv}uv + Y'_{u|w|}u|w| + Y'_{uw}uw) & M_3 &= \frac{1}{2}\rho L^3(M'_{u|v|}u|v| + M'_{uv}uv + M'_{u|w|}u|w| + M'_{uw}uw) \\
Z_3 &= \frac{1}{2}\rho L^2(Z'_{u|v|}u|v| + Z'_{uv}uv + Z'_{u|w|}u|w| + Z'_{uw}uw) & N_3 &= \frac{1}{2}\rho L^3(N'_{u|v|}u|v| + N'_{uv}uv + N'_{u|w|}u|w| + N'_{uw}uw)
\end{aligned}$$

- Submerged weight of the body and buoyancy force

$$\boldsymbol{F_g} = \begin{bmatrix} 0 & 0 & 0 & -B_W(z_g - z_b)\cos\theta\sin\phi & -B_W(z_g - z_b)\sin\theta & 0 \end{bmatrix}^T, \tag{6}$$

where B_W is the buoyance of the ROV. All the hydrodynamic coefficients are nondimensional by the water density ρ and length of the ROV L.

3. PMM tests

3.1. Test layout and installation

The prototype of the ROV model is a work-class ROV AUTO-1000 designed by AutoSubsea Vehicles Inc. The ROV model geometry, a 1:4 scale, 0.732 m long, 0.41 m width, and 0.45 m height, resin 3D printing hull with two manipulators, and all other device models, as shown in Figure 2. The gravity central is located 314 mm before the tail end and 244 mm above the bottom.

Figure 2. The ROV model.

Tests are conducted at the nonlinear wave channel of the Dalian University of Technology shown in Figure 3(b). The channel is 40 m long and 4 m wide and 1.8 m deep. The 6-DOF parallel platform was welded on the carriage which is fixed in the middle of the channel. The length between the ROV model and the inlet of current is 22 m. A Vectrino acoustic Doppler point current meter with a range of 4 m/s and a resolution of 1 mm/s was set after 18.5 m from the current inlet. A set of baffles were used to increase the current speed and for rectification. The front of the baffles is 18 m away from the ROV model and the width of the working area in the channel is 2 m. By considering the power of the pumps and the maximum current speed we need, the water depth is 1 m and the ROV model is in the middle in vertical. The water surface effect is limited according to the previous numerical studies[45]. The current was pumped by two axial flow pumps. Water flowed from an entrance on the ground ahead and inhaled into the exit 16 m after the ROV model. The length of the working area is long enough to obtain a steady speed of current.

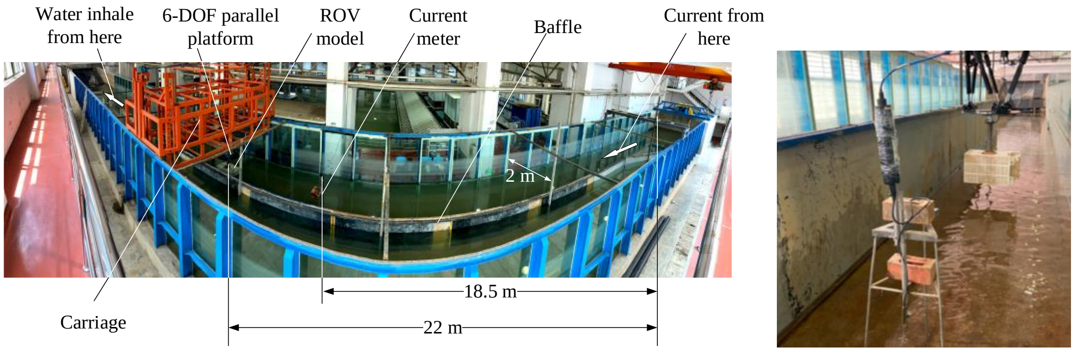

(a) (b)

Figure 3. The panorama of nonlinear wave channel (a) and the current meter (b).

The installation of the ROV model, the strut, the load cell, and the motion platform are shown in Figure 4. The origin *O* of the space-fixed coordinate system is fixed on the bottom center of the 6-DOF parallel platform (it is inverted). The Ox0 axis points to the longitudinal of the water channel and the Oy0 axis points to the lateral direction in the experiment. The load cell and the motion platform are connected with a thick steel plate which ensures the load cell is located at the control of the motion platform. The load cell is right above the gravity central of the ROV model in each installation method. The ROV model is linked by a steel strut with the load cell. To achieve 6-DOF forces and moments measurement without buoyancy and current direction effects, the ROV model needs to rotate. The installation of the load cell never changed in the whole experiment. We only change the connection type and direction of the strut and the ROV model. The installation for drag tests (+X cases) is illustrated in Figure 4(a), and the ROV model rotates 180° for −X cases. The methods in Figure 4(b) and (c) are for the drag tests in lateral (±Y) and vertical (±Z) respectively. The draft tests use the method in Figure 4(a). The drift angles are adjusted by rotating the motion platform on the Oz0 axis.

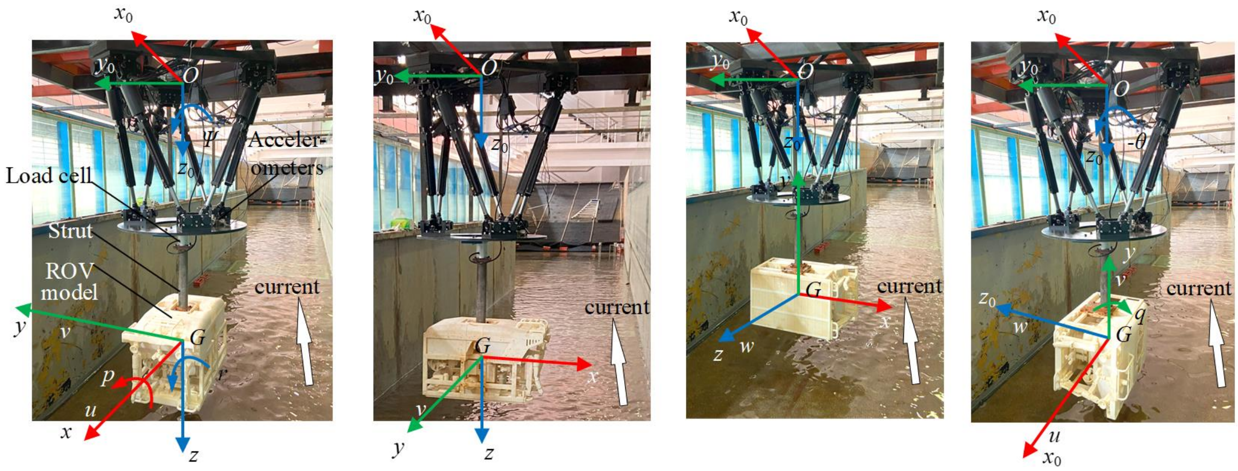

(a) (b) (c) (d)

Figure 4. The installation of the ROV model: longitudinal drag and horizontal PMM tests (a), lateral drag tests (b), vertical drag tests (c), and vertical PMM tests (d).

3.2. Test conditions

The PMM test abides the Froude's law of similarity. There are static drag tests and dynamic tests to estimate the viscous and inertia hydrodynamic coefficients. The static tests include the longitudinal drag, lateral drag, vertical drag, and drift drag tests. The ROV was fixed and The load time histories as the current scour of the ROV model were recorded. In the drift drag test, the ROV model was set to a settled angle in the horizontal plane. The dynamic tests include surge, pure sway, pure heave, pure roll, pure pitch, and pure yaw small amplitude PMM tests. The motion definition in the body-fixed coordinate system of each test and the coefficients calculated are listed in Tables 1 and 2. V_C indicates the magnitude of the current velocity varies from 0.2 to 0.5 m/s. The amplitude a=0.03m, and the frequency ω varies from 0.25 rad/s to 3.14 rad/s in the dynamic tests. The roll angle φ is 0.0872 rad, and the t indicates the physical time. The drift angles (β) are within ±20 ° and the trim angles (α) are in the range of ±10°. The details of the designed conditions are shown in Table 3.

Table 1. Static PMM tests names and their corresponding maneuvering derivatives.

Static tests	Longitudinal drag	±X	The current direction along the ±Ox axis	$X'_{u\|u\|}$ X'_{uu} $X'_{\|u\|}$ X'_{u} $Y'_{u\|u\|}$ Y'_{uu} $Y'_{\|u\|}$ Y'_{u} $Z'_{u\|u\|}$ Z'_{uu} $Z'_{\|u\|}$ Z'_{u} $K'_{u\|u\|}$ K'_{uu} $K'_{\|u\|}$ K'_{u} $M'_{u\|u\|}$ M'_{uu} $M'_{\|u\|}$ M'_{u} $N'_{u\|u\|}$ N'_{uu} $N'_{\|u\|}$ N'_{u}
	Lateral drag	±Y	The current direction along the ±Oy axis	$X'_{v\|v\|}$ X'_{vv} $X'_{\|v\|}$ X'_{v} $Y'_{v\|v\|}$ Y'_{vv} $Y'_{\|v\|}$ Y'_{v} $Z'_{v\|v\|}$ Z'_{vv} $Z'_{\|v\|}$ Z'_{v} $K'_{v\|v\|}$ K'_{vv} $K'_{\|v\|}$ K'_{v} $M'_{v\|v\|}$ M'_{vv} $M'_{\|v\|}$ M'_{v} $N'_{v\|v\|}$ N'_{vv} $N'_{\|v\|}$ N'_{v}
	Vertical drag	±Z	The current direction along the ±Oz axis	$X'_{w\|w\|}$ X'_{ww} $X'_{\|w\|}$ X'_{w} $Y'_{w\|w\|}$ Y'_{ww} $Y'_{\|w\|}$ Y'_{w} $Z'_{w\|w\|}$ Z'_{ww} $Z'_{\|w\|}$ Z'_{w} $K'_{w\|w\|}$ K'_{ww} $K'_{\|w\|}$ K'_{w} $M'_{w\|w\|}$ M'_{ww} $M'_{\|w\|}$ M'_{w} $N'_{w\|w\|}$ N'_{ww} $N'_{\|w\|}$ N'_{w}
	Drift	XY	The current direction has an included angle β against the -Ox axis	$X'_{u\|v\|}$ X'_{uv} $Y'_{u\|v\|}$ Y'_{uv} $Z'_{u\|v\|}$ Z'_{uv} $K'_{u\|v\|}$ K'_{uv} $M'_{u\|v\|}$ M'_{uv} $N'_{u\|v\|}$ N'_{uv}
	Trim	XZ	The current direction has an included angle α against the -Ox axis	$X'_{u\|w\|}$ X'_{uw} $Y'_{u\|w\|}$ Y'_{uw} $Z'_{u\|w\|}$ Z'_{uw} $K'_{u\|w\|}$ K'_{uw} $M'_{u\|w\|}$ M'_{uw} $N'_{u\|w\|}$ N'_{uw}

Table 2. Dynamic PMM tests names and their corresponding maneuvering derivatives.

Dynamic tests.	Surge	$u = V_C + a\omega\cos(\omega t)$, $\dot{u} = -a\omega^2\sin(\omega t)$, and other velocities are zero.	$X'_{\dot u}$ $Y'_{\dot u}$ $Z'_{\dot u}$ $K'_{\dot u}$ $M_{\dot u}$ $N'_{\dot u}$
	Sway	$u = V_C$, $v = a\omega\cos(\omega t)$, $\dot{v} = -a\omega^2\sin(\omega t)$, and other velocities are zero.	$X'_{\dot v}$ $Y'_{\dot v}$ $Z'_{\dot v}$ $K'_{\dot w}$ $M'_{\dot w}$ $N'_{\dot w}$
	Heave	$u = V_C$, $w = a\omega\cos(\omega t)$, $\dot{w} = -a\omega^2\sin(\omega t)$, and other velocities are zero.	$X'_{\dot w}$ $Y'_{\dot w}$ $Z'_{\dot w}$ $K'_{\dot w}$ $M'_{\dot w}$ $N'_{\dot w}$
	Roll	$u = V_C$, $\varphi = \varphi_0\sin(\omega t), p = \varphi_0\omega\cos(\omega t)$, $\dot{p} = -a\omega^2\sin(\omega t)$, and other velocities are zero.	$X'_{\dot p}$ $Y'_{\dot p}$ $Z'_{\dot p}$ $K'_{\dot p}$ $M'_{\dot p}$ $N'_{\dot p}$ X'_{p} Y'_{p} Z'_{p} K'_{p} M'_{p} N'_{p}
	Pitch	$u = V_C$, $q = \theta_0\omega\cos(\omega t)$, $\theta_0 = \arctan(a\omega / V_C)$, $\dot{q} = -\theta_0\omega^2\sin(\omega t)$, and other velocities are zero.	$X'_{\dot q}$ $Y'_{\dot q}$ $Z'_{\dot q}$ $K'_{\dot q}$ $M'_{\dot q}$ $N'_{\dot q}$ X'_{q} Y'_{q} Z'_{q} K'_{q} M'_{q} N'_{q}
	Yaw	$u = V_C$, $r = \Psi_0\omega\cos(\omega t)$, $\Psi_0 = \arctan(a\omega / V_C)$, $\dot{r} = -\Psi_0\omega^2\sin(\omega t)$, and other velocities are zero.	$X'_{\dot r}$ $Y'_{\dot r}$ $Z'_{\dot r}$ $K'_{\dot r}$ $M'_{\dot r}$ $N'_{\dot r}$ X'_{r} Y'_{r} Z'_{r} K'_{r} M'_{r} N'_{r}

Table 3. The details of the test conditions

Static tests	±X and ±Y cases	V_C/(m/s)	0.2, 0.25, 0.3, 0.35, 0.4, 0.45, 0.5
	±Z cases	V_C/(m/s)	0.2, 0.25, 0.3, 0.35, 0.4
	XY and XZ cases	V_C/(m/s) β and α/°	0.4 ±2, ±3, ±4, ±5, ±6, ±7, ±8, ±9, ±10
Dynamic tests	Surge and sway	V_C/(m/s) a/m ω/(rad/s)	0.4 0.03 0.25, 0.38, 0.50, 0.63, 1.26, 1.38, 1.51, 1.63, 1.76, 1.88, 2.20, 2.51, 2.83, 3.14
	Heave	VC/(m/s) a/m ω/(rad/s)	0.4 0.03 0.25, 0.38, 0.50, 0.63, 1.57, 1.88, 2.20, 2.51, 2.83, 3.14
	Roll	V_C/(m/s) φ/° ω/(rad/s)	0.4 5, 2 (5°: 0.25, 0.38, 0.50, 0.63), (2°: 1.26, 1.38, 1.51, 1.63, 1.76, 1.88, 2.20)
	Pitch and yaw	V_C/(m/s) a/m ω/(rad/s)	0.4 0.03 0.25, 0.38, 0.50, 0.63, 1.26, 1.38, 1.51, 1.63, 1.76, 1.88, 2.20

3.3. Test equipment

The PMM implemented in this study is a 6-DOF parallel platform, as shown in Figure 5(a). The maximum translation is ±189 mm in longitudinal, ±200 mm in lateral, and ±97 mm in vertical direction. The maximum orientation is 20°. Three accelerometers were installed to monitor and report the amplitude and frequency. Two horizontal sensors have a range of 1g and a resolution of 3×10^{-5}g. The range and resolution of the vertical sensor are 50g and 3×10^{-3}g respectively. Forces and moment were measured with a load cell of the six-component balance (KD461000N). Maximum force and moment ranges are 600 N for Fx, Fy, and 1000N for Fz and 300 N m for Mx, My, and 50 Nm for Mz, respectively as shown in Figure 6(a). The load cell was calibrated statically on a test stand using standard weights. The experimental data of forces were transferred to the body-fix coordinate system, and the hydrodynamic moments of gravity central were calculated according to the raw data. A steel strut as indicated in Figure 6(b) was designed to connect the load cell with the ROV model. The signal of the load cell and the accelerometers were synchronized and collected by the dynamic signal test and analysis system as shown in Figure 6(c). The force and moment from the load cell were transferred to the body-fixed coordinate system. The load cell was reset before each test. Each case of static test in one current speed contained at least 3 minutes. The measured current speed and hydrodynamic loads used to calculate derivatives in static tests were the average values after the signal was stable. We recorded the hydrodynamic loads in at last five periods of motions in PMM tests.

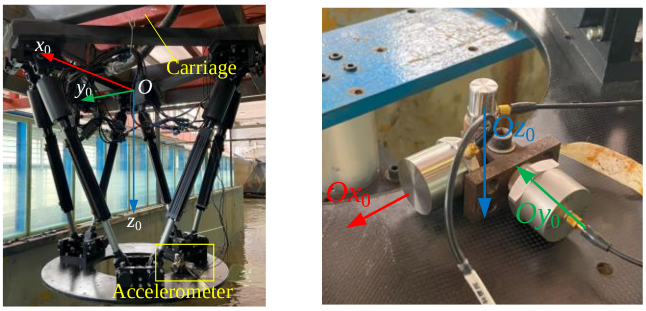

(a) (b)

Figure 5. The 6-DOF parallel platform (a) and the accelerometers (b).

(a) (b) (c)

Figure 6. The load cell (a), the strut (b), and the dynamic signal test and analysis system (c).

4. Experimental results

4.1. Hydrodynamic loads

The relative speeds between the ROV model and the current in the body-fixed coordinate system are used. It can indicate the motion velocity of the ROV. The ±X, ±Y, ±Z cases amount to the ROV in the longitudinal, lateral, and vertical motion with the motion speed equal to the current. To facilitate the analysis, the description of speed and motion direction are in the body-fixed coordinate system.

4.1.1 Static drag tests

The longitudinal static forces and moments of the ROV model in drag tests are shown in Figure 7(a) and (b). Most of the hydrodynamic forces and moments have a significant nonlinear trend with their velocities even when the speed is much less than the designed speed in the model scale which is about 0.4 m/s. The lateral force, roll moment, and yaw moment are more linear than other hydrodynamic forces and moments when the ROV is in a drag-link motion. The longitudinal drag is the largest load on the ROV model since it is collinear with motion speed. Other loads are quite obvious such as the vertical forces are more than 20% and 40% of the longitudinal drags in positive and negative Gx direction motion and the lateral forces are nearly 10% of the longitudinal drags in positive Gx direction motion. There are both roll, pitch, and yaw moments when the ROV moves in the longitudinal direction. The pitch moment is larger than the roll and yaw moments respectively.

As shown in Figure 7(c) and (d). Compared to the ±X cases, the difference is that the resistance is much larger in lateral motion than in the longitudinal and the roll moment has the same direction as motion speed in ±Y cases. The discrepancy of lateral force in −Y and +Y cases is less than 5%. The vertical force in rightward lateral motion is larger than in forward longitudinal motion, but it is only about 45% of the vertical force in backward longitudinal motion when the ROV has a leftward motion. As shown in Figure 7(e) and (f), the vertical motion has a great influence on the longitudinal force and yaw moment. In comparison with ±Y cases, the longitudinal forces increase more than that in ±Z cases at the same negative speed.

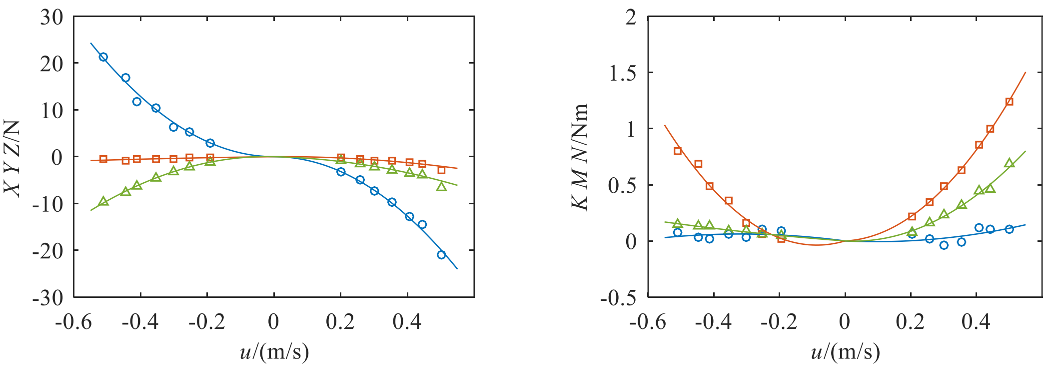

(a) (b)

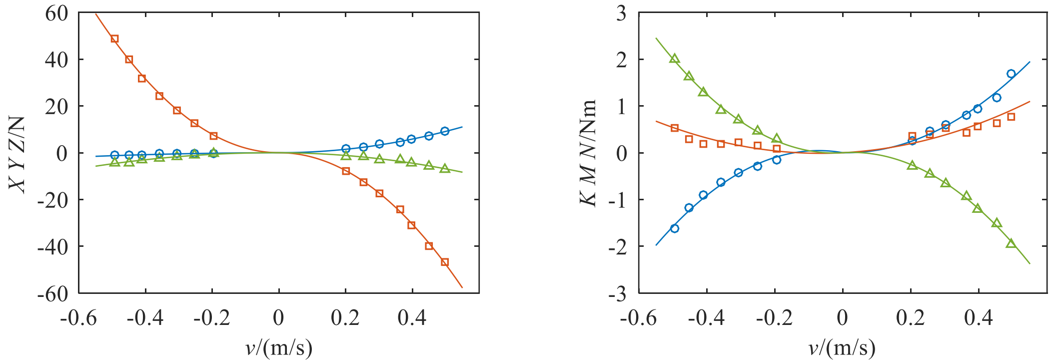

(c) (d)

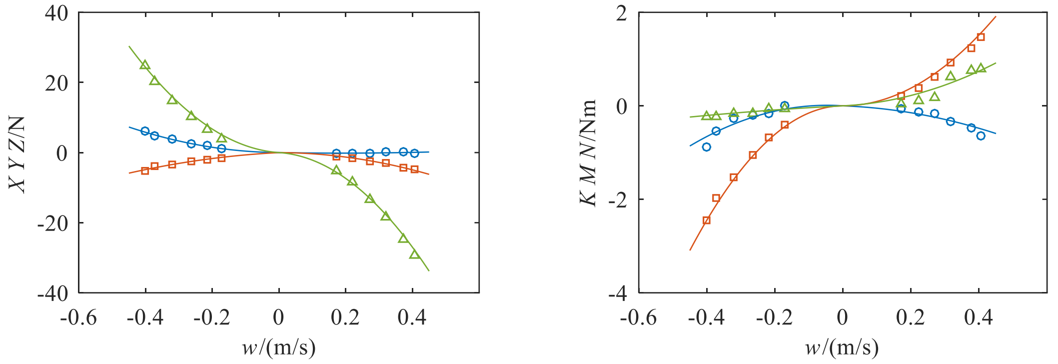

(e) (f)

Figure 7. The experimental results in static tests. The forces (a) and the moments(b) of ±X cases, the forces(c) and the moments(d) of ±Y cases, and the forces(e) and the moments(f) of ±Z cases.

4.1.2 Static drift and trim tests

The hydrodynamic forces and moments in drift tests are shown in Figure 8. The longitudinal and vertical force has little effect by the drift angle within ±10° as illustrated in Figure 8(a). The variation of the longitudinal and vertical force is less than 5% and 7% respectively. The longitudinal force increases slightly with the rising drift angle, especially when the drift angle is greater and zero. On the contrary, the vertical force decreases when the drift angle increases on the same side. A left drift motion occurs as a larger vertical hydrodynamic force is downward in the body-fixed coordinate system. The lateral force, roll, and yaw moment are sensitive to the drift angle as shown in Figure 8(b). There is a significant increment of pitch moment when the drift is greater than +6°, and the increasing ratio is larger than 5%. There is an obvious change in vertical force, roll, and pitch moment when the ROV model has a trim angle as shown in Figure 8(c) and (d). As the stern of the ROV model rises, the longitudinal force appears a limit decrease in which the changing ratio is less than 7%. The lateral force varies from the starboard to the port and then becomes stable with a ratio of less than 20% when the trim angle is greater than zero. There should be a zero lifting vertical force when the ROV has a trim angle of −4.04°. The direction of the roll moment is negative to the trim angle and the roll moments are almost equal at the same absolute values of the trim angle. There is a nonlinear trend arising to the pitch moment with a right over 3% variation ratio when the trim angle is larger than 6°. The yaw moment grew with a ratio of nearly 4%, but it began to level off as the trim angle was greater than 4°.

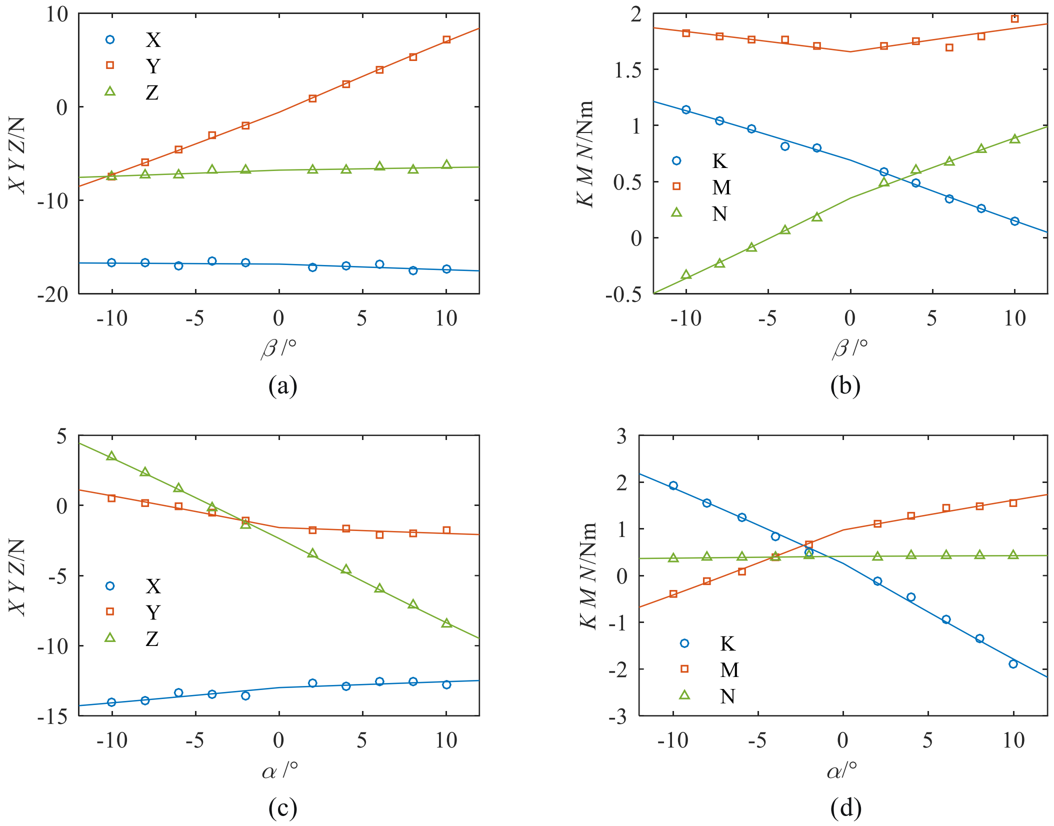

Figure 8. Hydrodynamic load in the drift (a) (b) and trim (c) (d) drag tests.

4.1.3 Dynamic tests

Hydrodynamic force and moments are shown in their hysteresis loops in Figure 9 including the longitudinal force in surge tests, the lateral force in sway tests, the vertical force in heave tests, the roll moment in pure roll tests, the pitch moment in pure pitch tests, and the yaw moment in pure yaw tests. The loops in this section show the relationship between hydrodynamic loads and oscillation displacement.

The longitudinal, lateral, and vertical displacements are adopted in surge, sway, and heave tests. The roll, pitch, and yaw angles are chosen in pure roll, pitch, and yaw tests. The displacements change as a sine function with an amplitude of 0.03 m, and the angles are the cosine function in which the amplitudes of pitch and yaw increase with the oscillation frequencies. The hysteresis loop shows the variation of inertia and viscous forces. The acceleration shares the same phase as the displacement so the acceleration approaches the maximum as the meantime of displacement, and the velocity is the opposite. Therefore, there is only the inertia and viscous load when the displacement is the maximum and zero respectively. As shown in these figures, the inertia load increases with the frequency growth. The difference between the upper and lower values of the same curve increases with the oscillation frequency when the displacement reaches the equilibrium position which indicates an increasing viscous force. The average values of these loads are not zero because the ROV model encounters 6 DOF hydrodynamic loads. The hydrodynamic load curves are twisty when the ROV model oscillates at low frequencies due to the unsteady flow and this phenomenon disappears as the frequency rises.

The historical loops for the part of cross-coupling hydrodynamic loads are shown in Figure 10. There are the largest moment coefficients in the surge, sway, and heave tests and the force coefficients in the roll, pitch, and yaw tests. The moments in low frequencies vary nonlinearly with oscillation amplitude. The values of the hydrodynamic moments and forces have a significant difference when the ROV model translates to the position with the same acceleration amplitude but opposite phase.

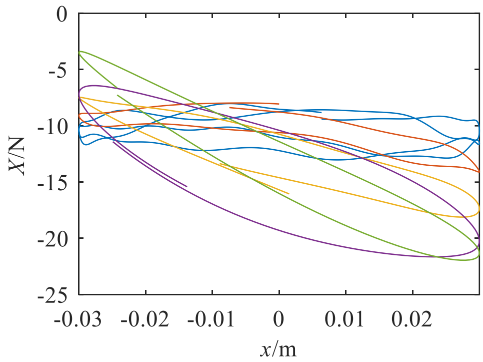

(a) The longitudinal force in surge tests

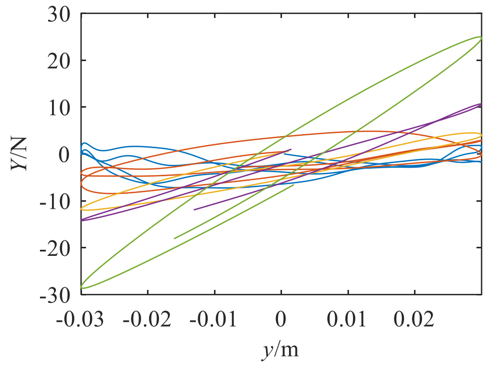

(b) The lateral force in sway tests

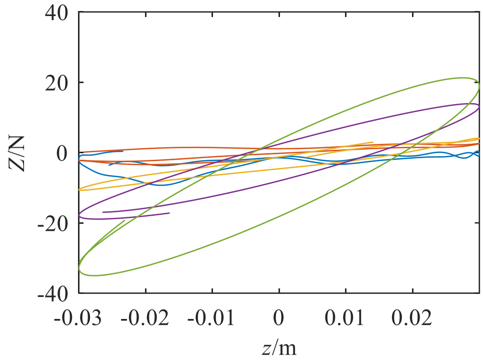

(c) The vertical force in heave tests

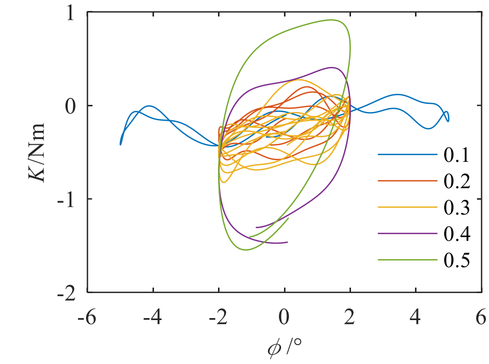

(d) The roll moment in roll tests

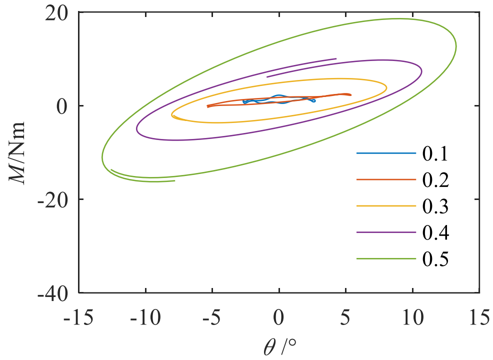

(e) The pitch moment in pure pitch tests

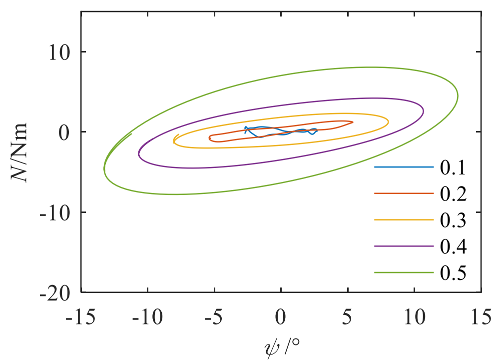

(f) The yaw moment in pure yaw tests

Figure 9. The hysteresis loops of the hydrodynamic force and moments in dynamic tests.

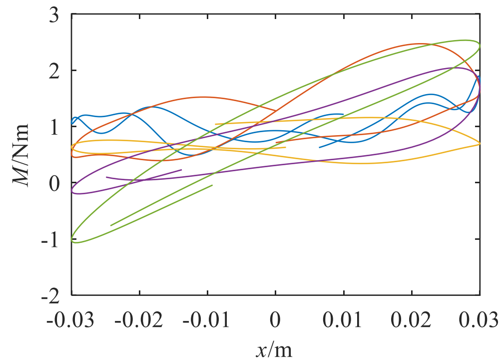

(a) The pitch moment in surge tests

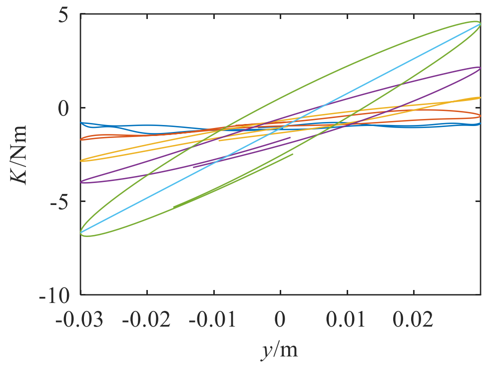

(b) The roll moment in sway tests

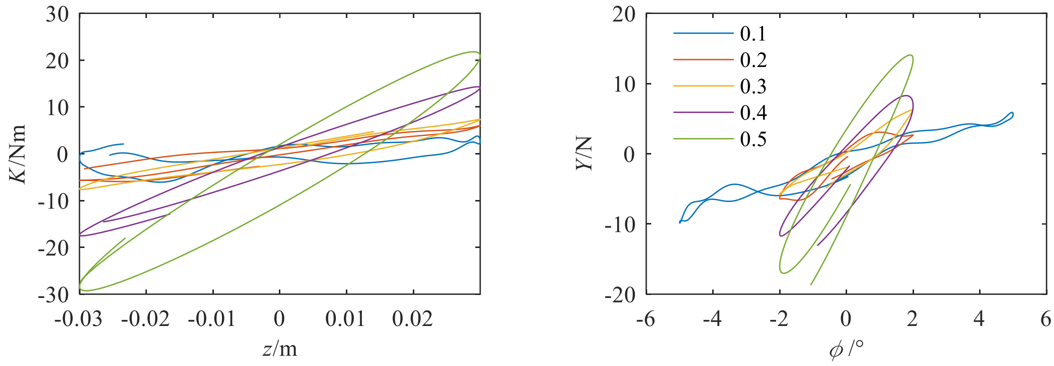

(c) The roll moment in heave tests (d) The lateral force in roll tests

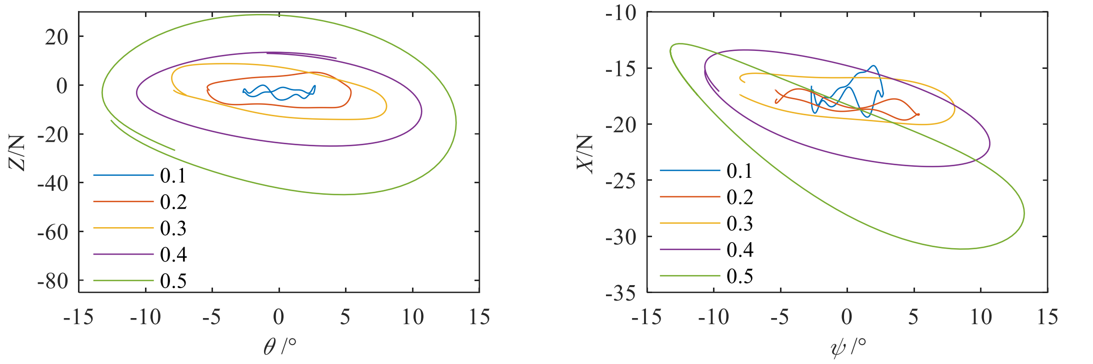

(e) The vertical force in pure pitch tests (f) The longitudinal force in pure yaw tests

Figure 10. The historical loops for the part of cross-coupling hydrodynamic loads

4.2. Hydrodynamic coefficients

4.2.1. Static tests

The data of each hydrodynamic load in static tests are fitted to a quadratic absolute value function $F = F_{\varsigma|\varsigma|}\varsigma|\varsigma| + F_{\varsigma\varsigma}\varsigma^2 + F_{|\varsigma|}|\varsigma| + F_{\varsigma}\varsigma$ where F is the hydrodynamic loads and ς is the current velocities of each case in the body-fixed coordinate system. The non-dimensional coefficients are calculated via $F_{\varsigma|\varsigma|}$, $F_{\varsigma\varsigma}$, $F_{|\varsigma|}$, and F_{ς} according to equation (4). Nonlinear non-dimensional coefficients are shown in Figure 11. All the nonlinear hydrodynamic forces and moments coefficients ($F_{\varsigma|\varsigma|}$ and $F_{\varsigma\varsigma}$) were divided by $\frac{1}{2}\rho L^2$ and $\frac{1}{2}\rho L^3$ respectively. There are greater values of $X'_{u|u|}$, $Y'_{v|v|}$, $Z'_{w|w|}$, $K'_{v|v|}$, $M'_{w|w|}$, $N'_{v|v|}$ for each motion direction which agrees with the relative size of values for hydrodynamic loads.

The velocity coupling coefficients were estimated via equation (5) and the non-dimensional method is the same as $F_{\varsigma|\varsigma|}$. The hydrodynamic loads coincident with the static drag test results were subtracted. Compared to the drift angle, the trim angle increases the longitudinal force. There is a significant effect on lateral and vertical hydrodynamic forces by drift and trim motion. The nonlinear coefficients of lateral and vertical forces in drift and trim motion (Y_{uv} and Y_{zw}) are greater than their nonlinear coefficients with only respect to the lateral and vertical speeds. The vertical force is more sensitive to the trim angle than other forces as Z_{uw} is nearly twice of $Z_{w|w|}$. The trim angle has an obvious impact on roll and pitch moments, and the drift angle influences the yaw moment more than other moments. For all velocity coupling coefficients, the coefficients relative to uw and uv will be the greatest in each DOF for drift and trim motion.

The Taylor expansion was applied in modeling the hydrodynamic model, therefore linear hydrodynamics were maintained. To compare the linear and nonlinear coefficients, $\sqrt{gL}$ which has the same order as the velocity was chosen to normalize the linear coefficients because Froude's law of similarity was abided by. The linear hydrodynamic coefficients of forces and moments were divided by $\frac{1}{2}\rho L^2\sqrt{gL}$ and $\frac{1}{2}\rho L^3\sqrt{gL}$ respectively. The velocity of the largest coefficient in each DOF is not exactly the same as the nonlinear coefficients. X'_w, $Y'_{|w|}$, Z'_w, $K'_{|w|}$, $M'_{|v|}$, N'_v are the greatest linear coefficients in each DOF.

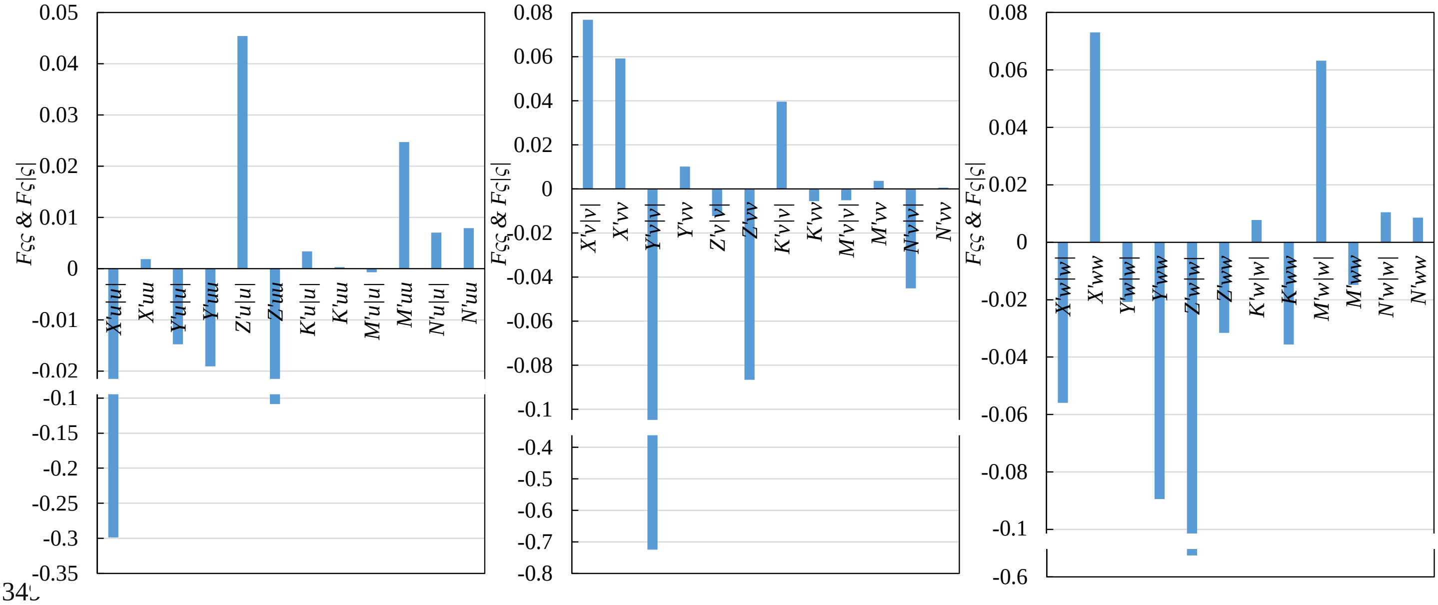

(a)

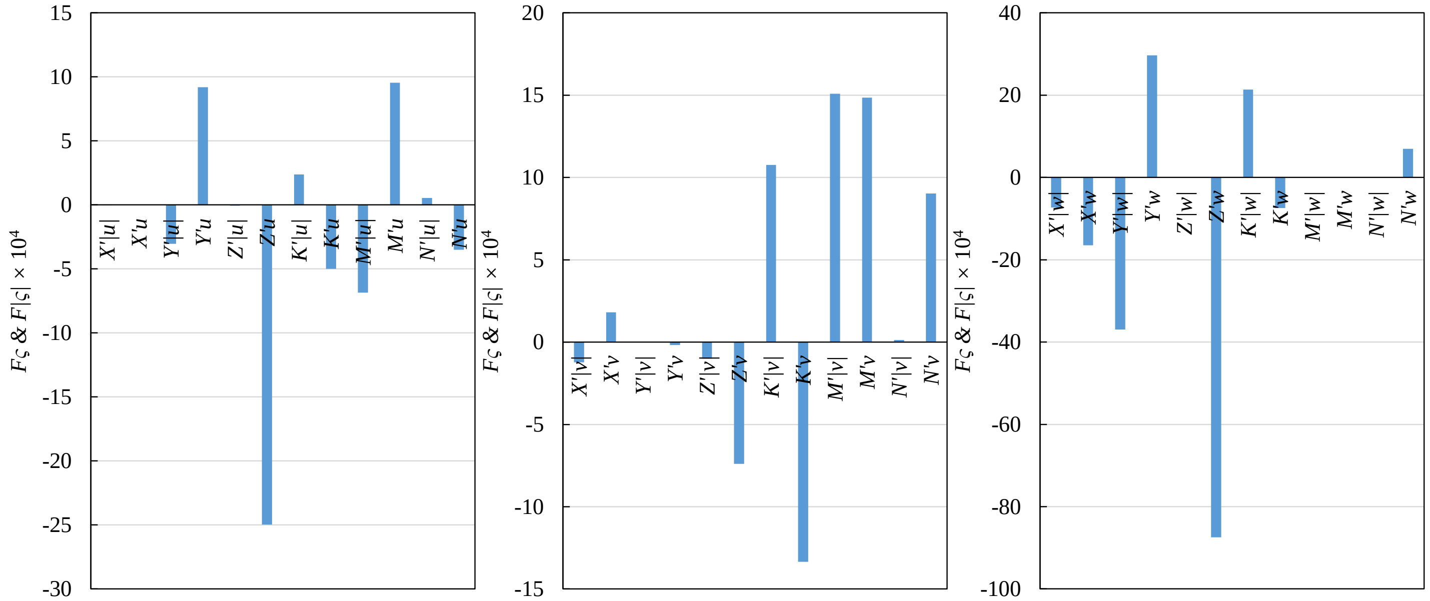

(b)

Figure 11. Nonlinear hydrodynamic coefficients (a) and linear coefficients (b) of static tests

4.2.2. Dynamic tests

To filter the turbulent flow and mechanical vibration effect on inertia hydrodynamic coefficients, a band-pass filter with the frequency band 0.9ω<ω <1.1ω (ω is the motion frequency) is therefore considered [24]. The velocity and acceleration terms in the equations can be represented as listed in Table 2. Equation (1) and (3) can be rewritten as follows:

In surge tests: $X + m\dot{u} = 1/2\rho L^3 X'_{\dot{u}}\dot{u} + X_D u$, $Y = 1/2\rho L^3 Y'_{\dot{u}}\dot{u} + Y_D u$, $Z = 1/2\rho L^3 Z_{\dot{u}}{}'\dot{u} + Z_D u$,

$K = 1/2\rho L^4 K_{\dot{u}}{}'\dot{u} + K_D u$, $M = 1/2\rho L^4 M_{\dot{u}}{}'\dot{u} + M_D u$, $N = 1/2\rho L^4 N_{\dot{u}}{}'\dot{u} + N_D u$, Sway tests: $X = 1/2\rho L^3 X_{\dot v}{}'\dot v + X_D v$, $Y + m\dot v = 1/2\rho L^3 Y_{\dot v}{}'\dot v + Y_D v$, $Z = 1/2\rho L^3 Z_{\dot v}{}'\dot v + Z_D v$, $K = 1/2\rho L^4 K_{\dot v}{}'\dot v + K_D v$, $M = 1/2\rho L^4 M_{\dot v}{}'\dot v + M_D v$, $N = 1/2\rho L^4 N_{\dot v}{}'\dot v + N_D v$,

Heave tests: $X = 1/2\rho L^3 X_{\dot w}{}'\dot w + X_D w$, $Y = 1/2\rho L^3 Y_{\dot w}{}'\dot w + Y_D w$, $Z + m\dot w = 1/2\rho L^3 Z_{\dot w}{}'\dot w + Z_D w$, $K = 1/2\rho L^4 K_{\dot w}{}'\dot w + K_D w$, $M = 1/2\rho L^4 M_{\dot w}{}'\dot w + M_D w$, $N = 1/2\rho L^4 N_{\dot w}{}'\dot w + N_D w$,

Roll tests: $X = 1/2\rho L^4 X_{\dot p}{}'\dot p + 1/2\rho L^2 \sqrt{gl} X_p{}' p$, $Y = 1/2\rho L^4 Y_{\dot p}{}'\dot p + 1/2\rho L^2 \sqrt{gl} Y_p{}' p$, $Z = 1/2\rho L^4 Z_{\dot p}{}'\dot p + 1/2\rho L^2 \sqrt{gl} Z_p{}' p$, $K + I_x\dot p + B_W(z_g - z_b)\sin\varphi = 1/2\rho L^5 K_{\dot p}{}'\dot p + 1/2\rho L^3 \sqrt{gl} K_p{}' p$, $M = 1/2\rho L^5 M_{\dot p}{}'\dot p + 1/2\rho L^3 \sqrt{gl} M_p{}' p$, $N = 1/2\rho L^5 N_{\dot p}{}'\dot p + 1/2\rho L^3 \sqrt{gl} N_p{}' p$,

Pitch tests: $X = 1/2\rho L^4 X_{\dot q}{}'\dot q + 1/2\rho L^2 \sqrt{gl} X_q{}' q$, $Y = 1/2\rho L^4 Y_{\dot q}{}'\dot q + 1/2\rho L^2 \sqrt{gl} Y_q{}' q$, $Z = 1/2\rho L^4 Z_{\dot q}{}'\dot q + 1/2\rho L^2 \sqrt{gl} Z_q{}' q$, $K = 1/2\rho L^5 K_{\dot q}{}'\dot q + 1/2\rho L^3 \sqrt{gl} K_q{}' q$, $M + I_y\dot q = 1/2\rho L^5 M_{\dot q}{}'\dot q + 1/2\rho L^3 \sqrt{gl} M_q{}' q$, $N = 1/2\rho L^5 N_{\dot q}{}'\dot q + 1/2\rho L^3 \sqrt{gl} N_q{}' q$,

Yaw tests: $X = 1/2\rho L^4 X_{\dot r}{}'\dot r + 1/2\rho L^2 \sqrt{gl} X_r{}' r$, $Y = 1/2\rho L^4 Y_{\dot r}{}'\dot r + 1/2\rho L^2 \sqrt{gl} Y_r{}' r$, $Z = 1/2\rho L^4 Z_{\dot r}{}'\dot r + 1/2\rho L^2 \sqrt{gl} Z_r{}' r$, $K = 1/2\rho L^5 K_{\dot r}{}'\dot r + 1/2\rho L^3 \sqrt{gl} K_r{}' r$, $M = 1/2\rho L^5 M_{\dot r}{}'\dot r + 1/2\rho L^3 \sqrt{gl} M_r{}' r$, $N + I_z\dot r = 1/2\rho L^5 N_{\dot r}{}'\dot r + 1/2\rho L^3 \sqrt{gl} N_r{}' r$.

The reason why we ignore the high-order hydrodynamic coefficients is that the amplitude of these tests is limited and the oscillation velocities are far less than 1. Besides, the bandpass filter excludes the double and triple-frequency components which are related to the high-order hydrodynamic coefficients in the frequency domain. The longitudinal velocity in each test could be seen as a constant equal to the current velocity, therefore the hydrodynamic Coriolis–Centripetal loads which correlate to the longitudinal velocity and angular velocities should be considered.

The equations of surge, sway, and heave could be transformed into a form of $F = F_{in}\sin(\omega t) + F_{out}\cos(\omega t) + F_{static}$ where F is the load data that the force ring measured but do not include the mass and moment of inertia. F_{in} is related to the inertia hydrodynamic coefficient and the amplitude of the acceleration, and F_{out} is the product of the viscous hydrodynamic coefficients and the amplitude of the oscillation velocity. The least square method was used to fit the function. F_{in} of the surge, sway, and heave tests in several frequencies are shown in (a)

(b) (c)

Figure 12. The sine term increases linearly with the accelerations. Except the acceleration has a significant influence on the force along the oscillation direction, there are greater sine terms in each case such as yaw moment in surge motion, roll moment in sway motion, and lateral force in heave motion.

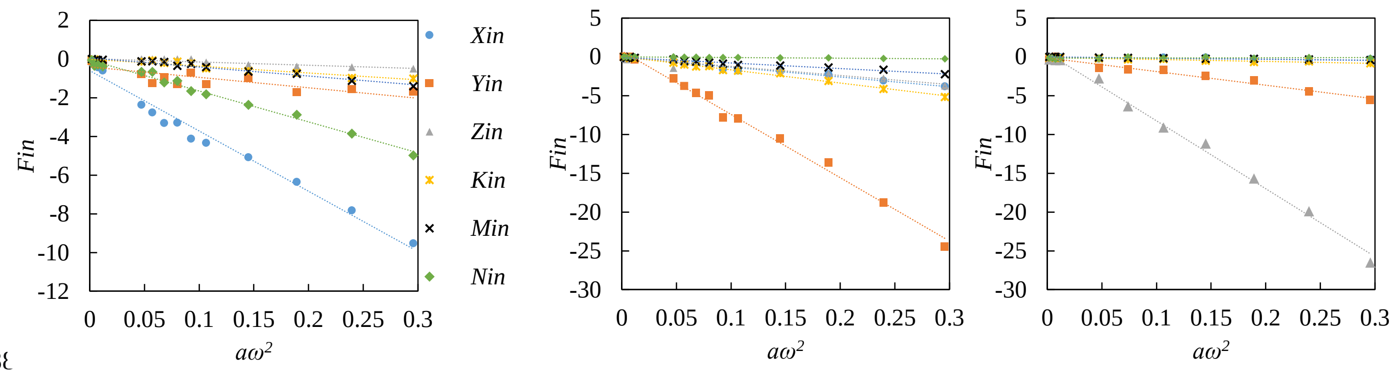

(a) (b) (c)

Figure 12. The coefficient of the sine terms of the surge (a), sway (b), and heave (c) tests.

The hydrodynamic load in roll, pitch, and yaw tests can be expressed as $F = F_{\text{in}}\cos(\omega t) + F_{\text{out}}\sin(\omega t) + F_{\text{static}}$ where the meaning of each term is the same as we mentioned above, and the data of each hydrodynamic load in roll, pitch, and yaw tests are fitted to that function. As shown in Figure 13(a), the lateral force and roll moment show a significant linear relation with increasing sway acceleration, but there is a variation in other loads. Figure 13(b) and (c) presents the variation of the cosine term of pure pitch and yaw motion against the accelerations. The pitch and yaw acceleration increases the inertial hydrodynamic loads dramatically in which the vertical force and the pitch moment in pitch motion and longitudinal force and the yaw moment in yaw motion change particularly compared to the roll motion. The sine term F_{out} against the rotational velocities is shown in (a)

(b) (c)

Figure 14.

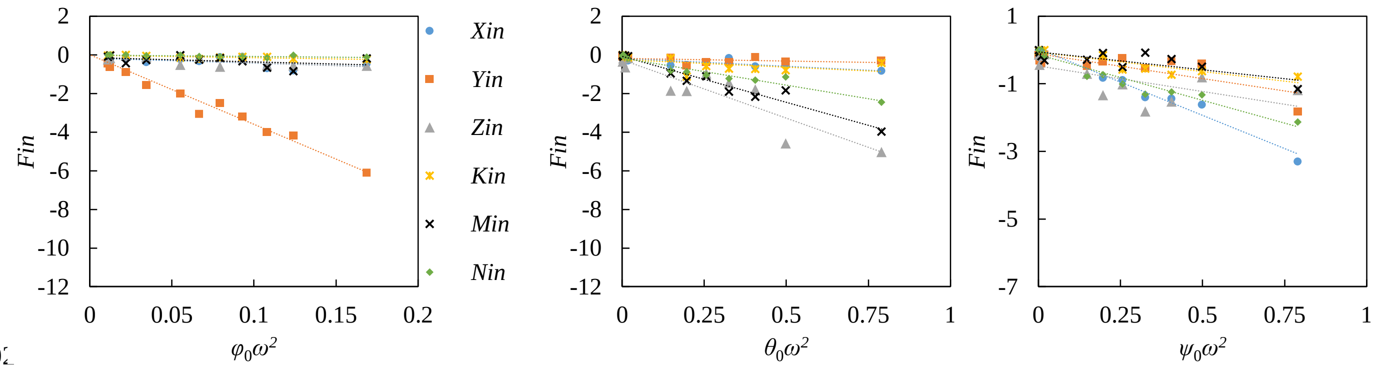

(a) (b) (c)

Figure 13. The coefficients of the cosine terms of the roll (a), pitch (b), and yaw (c) tests.

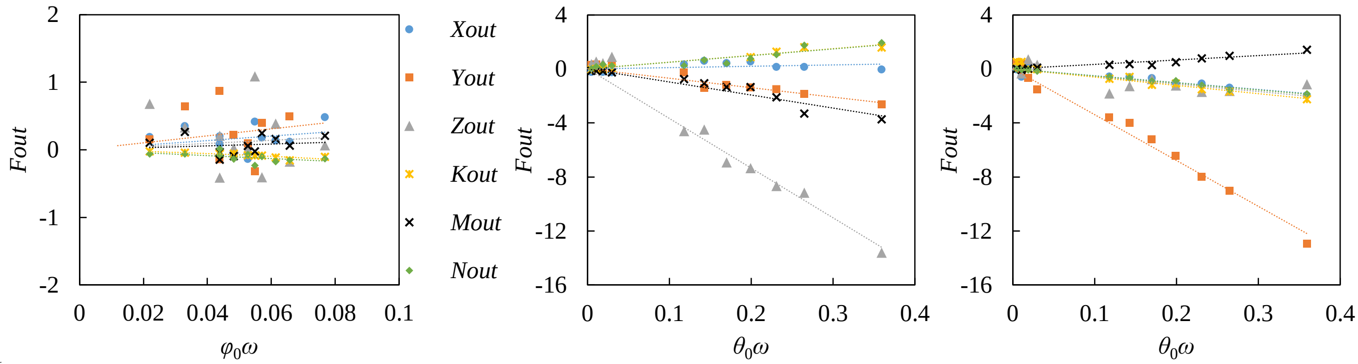

(a) (b) (c)

Figure 14. The coefficients of the sine terms of the roll (a), pitch (b), and yaw (c) tests.

The least square method was used to estimate the inertia coefficients which should be the slope between F_{in} and the accelerations. The inertia coefficients are shown in Figure 15. To compare the relative size of the inertia coefficients, the non-dimensional mass of the prototype was calculated as 0.066. for the inertia coefficients in the leading diagonal of the added mass matrix of the ROV, the difference between the lateral and vertical inertia is less than 15% of the mass but they are over twice larger than the longitudinal inertia. The inertia coefficients of rotational motion have the same rules but the inertia is less than 14% of the mass. There are considerable values of inertia coefficients in off-diagonal. There are coefficients more than 10% of the mass, such as $X_{\dot{v}}$, $X_{\dot{r}}$, $Y_{\dot{u}}$, $Y_{\dot{w}}$, $Y_{\dot{p}}$, $Z_{\dot{v}}$, $Z_{\dot{q}}$, $K_{\dot{u}}$, $K_{\dot{v}}$, $M_{\dot{u}}$, $M_{\dot{v}}$, and $N_{\dot{u}}$. As shown in Figure 16, the non-dimensional viscous coefficients to the rotational velocities are greater than those to the linear velocities.

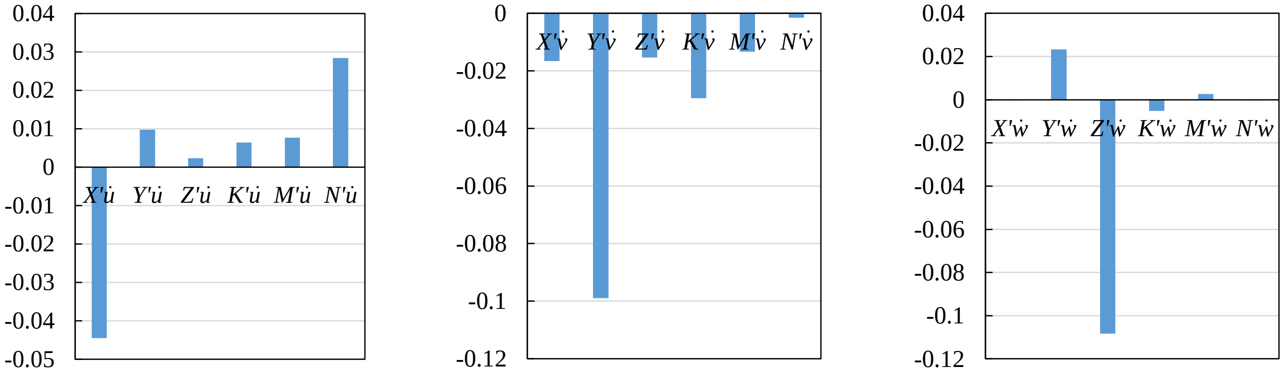

(a)

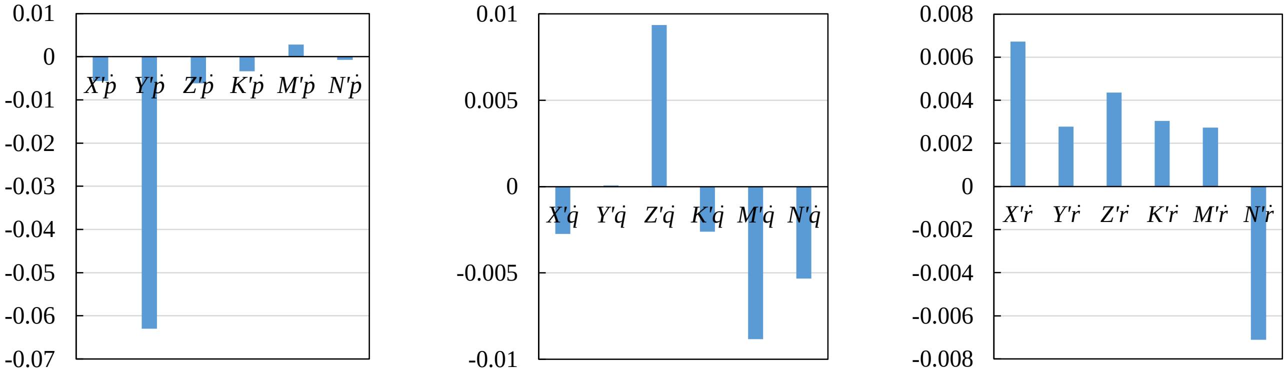

(b)

Figure 15. The non-dimensional inertia coefficients of linear (a) and angular acceleration (b).

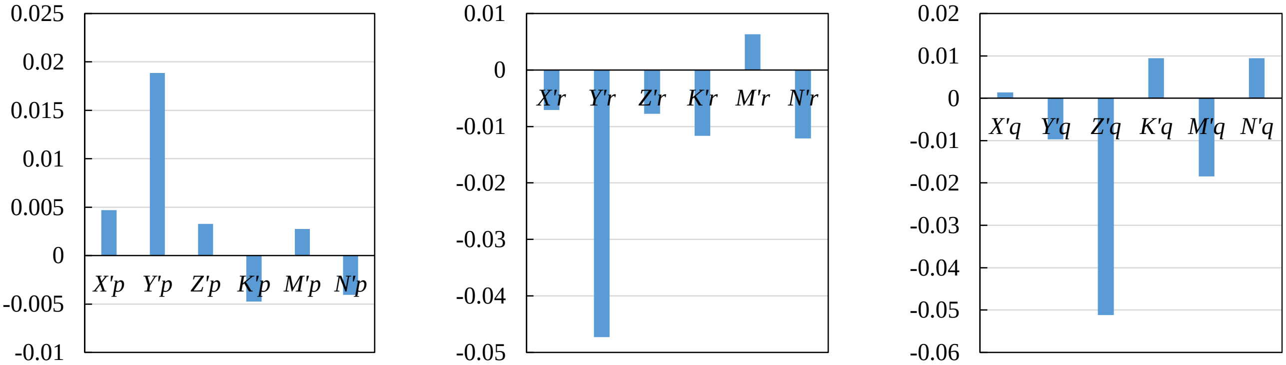

Figure 16. The non-dimensional viscous coefficients to the angular velocities of the ROV

5. Sensitivity analysis

There are mathematical models of ROV in existing literature. However, the choice of the pivotal hydrodynamic coefficients does not reach a coincident procedure. The presented sensitivity analysis methods are suitable for a work-class ROV, but the typical trajectories did not stipulate, and the effect of different trajectories of ROV was not studied. The motion form of an ROV shows a significant difference from ships or submarines. A work-class ROV seldom navigates at its design speed, or in a uniform speed motion with a typical velocity. Besides, a smaller hydrodynamic in some DOFs may still be important because a work-class ROV can move along all 6DOF due to the overdriven propeller distribution. Therefore, it is not an appropriate method that focus on one main moving direction to decide the impact of hydrodynamic coefficients with steady motion.

To investigate the sensitivity of the hydrodynamic coefficient of the work-class ROV, the Normalized Sensitivity Coefficient (NSC) of the ROV was presented [46, 47]. NSC allows the rational comparison of parameters whose order of magnitude could be significantly different. The NSC indicates the influence of coefficient X_i on load Y_i is defined as follows:

$$\mathrm{NSC}_X = \frac{\sum_{i=1}^{\mathrm{N}} \left(\frac{\Delta Y_i}{\bar{Y}_i} \frac{\bar{X}_i}{\Delta X_i} \right)}{\mathrm{N}} \tag{7},$$

where ΔY_i and ΔX_i is the variation of the load and the coefficient. $\bar{X}_i$ and $\bar{Y}_i$ is the estimated value of the coefficient and average of the load. Three kinds of trajectories were chosen to compare the difference between NSCs including the drag motion, the drift motion, and the stationary random motion. The change of the coefficients according to the normal distribution with the mean value of the estimated value and with the standard deviation for 50% of the coefficients. Therefore, we have N random ΔX_i and corresponding ΔY_i at one motion kind. The average of each $\left(\frac{\Delta Y_i}{\bar{Y}_i} \frac{\bar{X}_i}{\Delta X_i} \right)$ indicates the sensitivity of the coefficient at that motion. This method aims to investigate the trajectory effect on the sensitivity of the hydrodynamic coefficients.

5.1. Drag motion

In the drag motion, the hydrodynamic coefficient changes once a time. Only one velocity of *u*, *v*, and *w* is nonzero in one case. The range of the velocity is from −1.1~1.1 m/s and −0.9~0.9 m/s which includes the design speed of ±*Ox*, ±*Oy*, and ±*Oz* directions. The sensitivity of force coefficients in equation (4) with different linear velocities is shown in Figure 17. For most cases, the NSCs of the second-order coefficients are much larger than first-order'. The sensitivity of first-order coefficients decreases with the increasing velocity. However, it should be noted that the difference of the NSCs of $X_{w|w|}$, X_{ww}, and X_w is less than 5% when the vertical velocity is 0.4 m/s. The NSC of Y_u is larger than the second-order coefficients' as the absolute lateral velocity is less than 0.2 m/s. The NSC of $Y_{w|w|}$ and Y_{ww} decreases with increasing speed, and the NSC of $Y_{w|w|}$ is smaller than two linear coefficients when the vertical velocity is less than 0.4 m/s. The sensitivity of Z_u is larger than $Z_{u|u|}$ at low speed, and it is the same as Z_v. The sensitivity of Z_w increases sharply as the vertical speed decreases, and it is greater than Z_{ww} as the absolute vertical speed is less than 0.7 m/s. The NSC of the moment coefficients in equation (4) are shown in Figure 18. Besides $M_{w|w|}$ and M_w, the second-order coefficients have no advantage in their sensitivity. The linear coefficients are more sensitive than high orders at low speeds. K_{uu}, $M_{u|u|}$, and N_{vv} are less than the linear coefficients of the same motion.

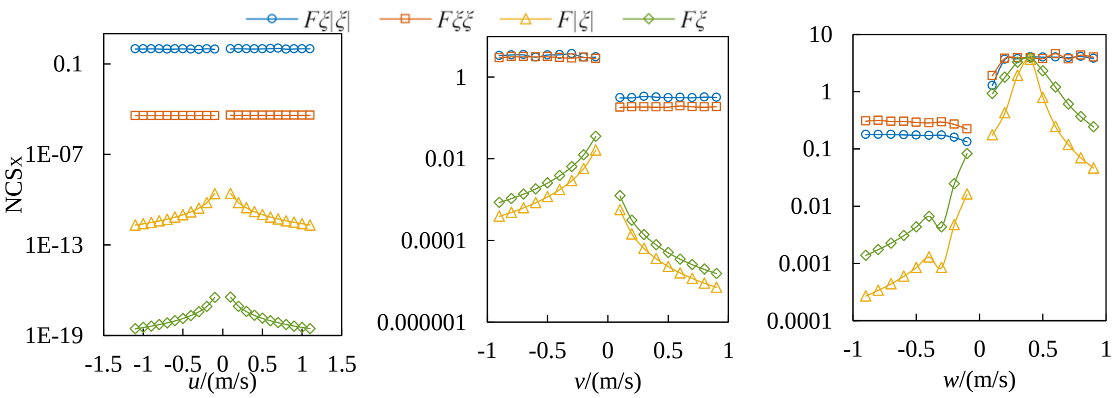

(a)

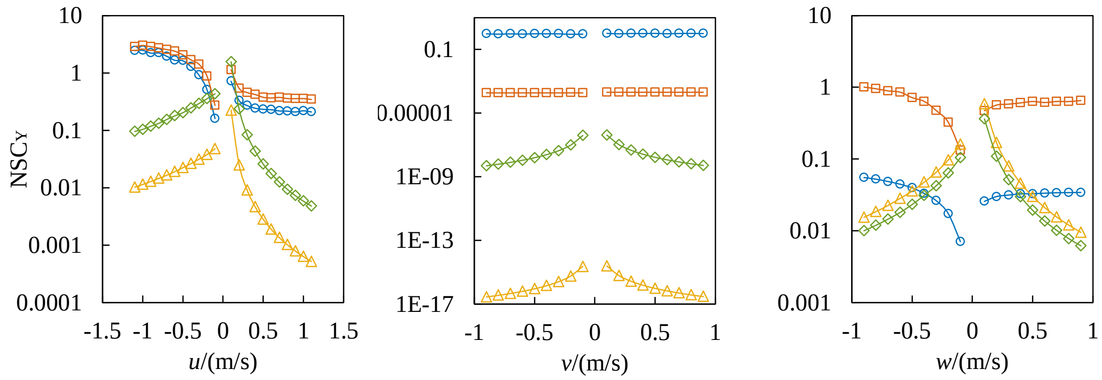

(b)

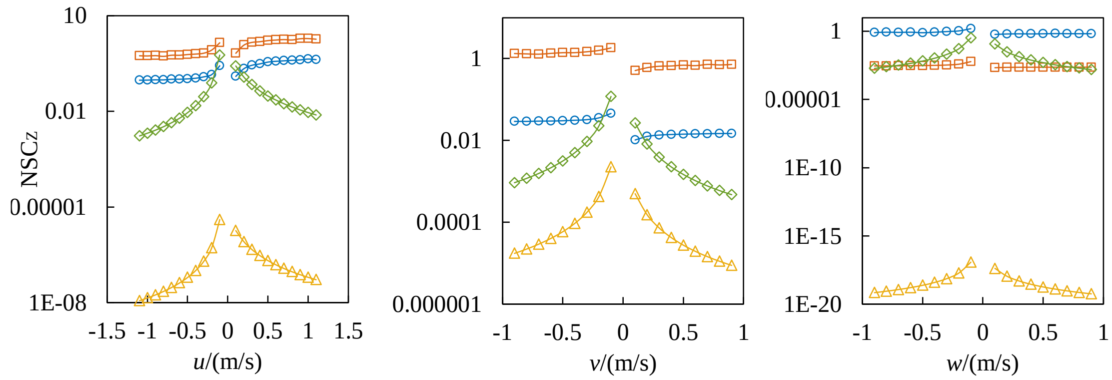

(c)

Figure 17. The NSCs of longitudinal forces (a), lateral forces (b), and vertical forces (c) against the velocity in drag motion

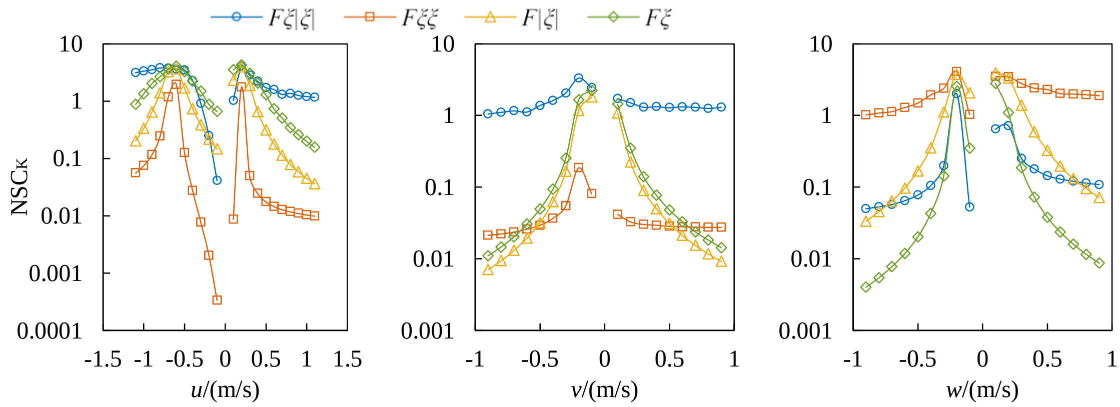

(a)

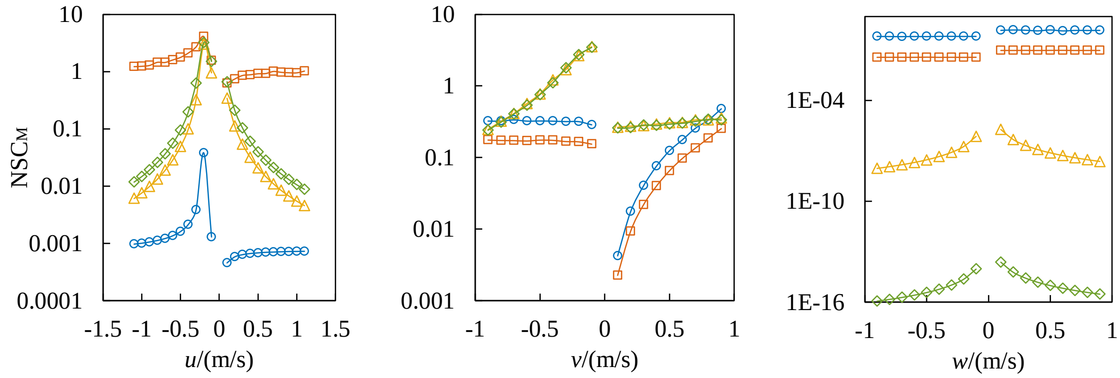

(b)

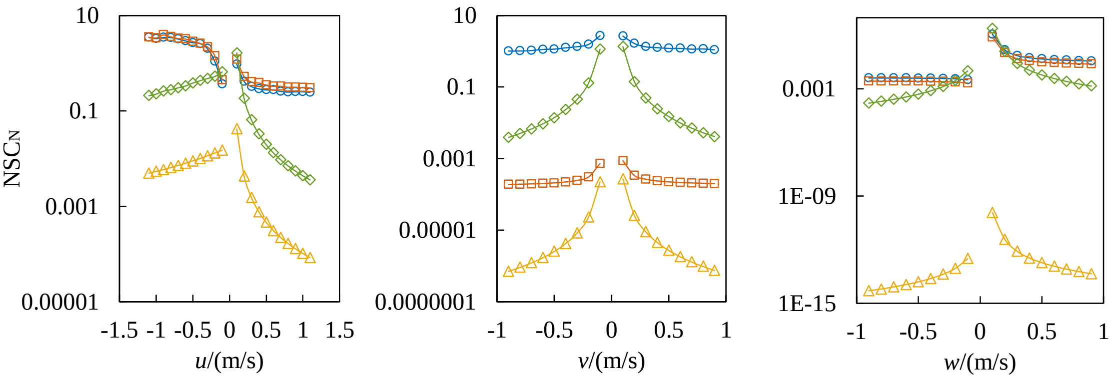

(c)

Figure 18. The NSCs of roll (a), pitch (b), and yaw moment (c) against the velocity in drag motion.

5.2. Drift motion

The drift motion aimed to study the sensitivity of coupling hydrodynamic coefficients. The NSCs of coupling force coefficients are shown in Figure 19. Each case includes two NSCs under 5 longitudinal velocities and one lateral velocity. The longitudinal speed in each case rises from 0.8 m/s to 1 m/s with an interval of 0.2 m/s. 10 different lateral velocities (cases 1 to 10) from 0.01 m/s to 0.1 m/s with an interval of 0.01 m/s are adopted. And 10 different lateral velocities from −0.01 m/s to −0.1 m/s with an interval of −0.01 m/s are chosen for cases 11 to 20. The NSC increases with the lateral velocities. The lateral moving direction has a limited influence on the sensitivity of force coefficients. The sensitivity of $F_{\xi\zeta}$ is greater than $F_{\xi|\zeta|}$. The NSC of lateral force decreases with the increasing vertical velocity at a low longitudinal speed when the ROV moves to the Oy direction. The sensitivity of vertical force coefficients decreases with increasing vertical velocity.

The NSC will grow when the longitudinal speed of 0.6 m/s. Two conditions should be noted that the sensitivity of the coefficient $F_{\xi|\zeta|}$ become larger than $F_{\xi\zeta}$ when the longitudinal velocity of 0.8 m/s and 0.4 m/s and vertical velocity of 0.09 and 0.04 m/s. Therefore, both coefficients Y_{uw}, $Y_{u|w|}$, Z_{uw}, and $Z_{u|w|}$ should not be ignored.

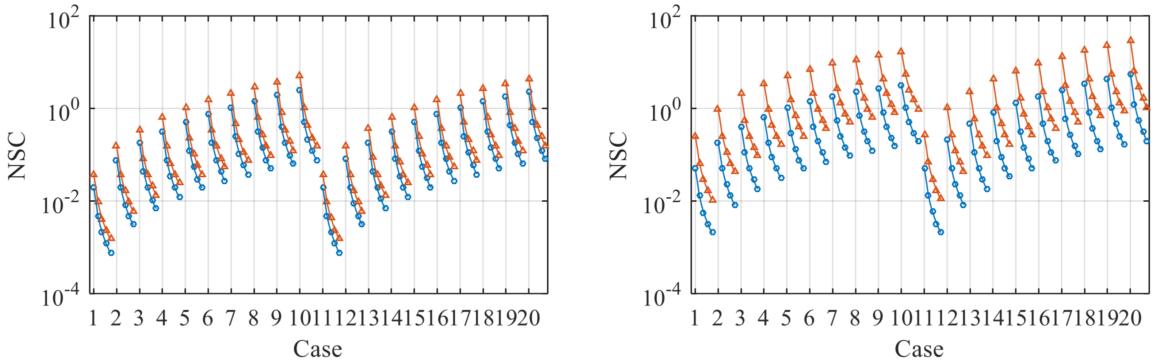

(a) The NSC of *Xuv* and *Xu*|*v*| (b) The NSC of *Xuw* and *Xu*|*w*|

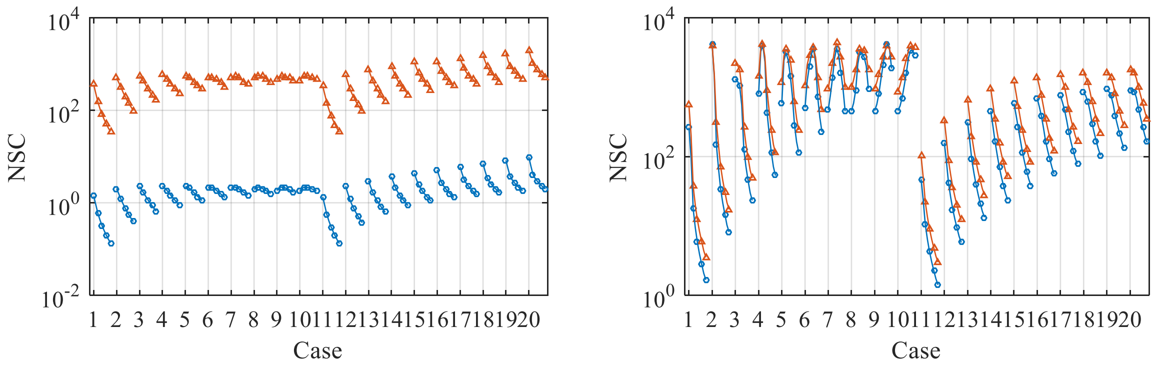

(c) The NSC of *Yuv* and *Yu*|*v*| (d) The NSC of *Yuw* and *Yu*|*w*|

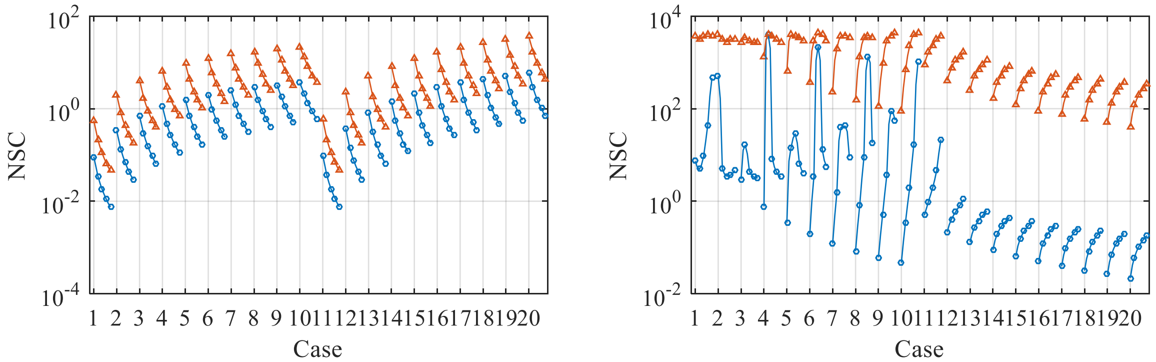

(e) The NSC of *Zuv* and *Zu*|*v*| (f) The NSC of *Zuw* and *Zu*|*w*|

Figure 19. The NSCs of coupling force coefficients against the velocity in drift motion. Each data point indicates an NSC of a sort of coupling velocity. The longitudinal velocity of each data point of one curve from left to right is 0.2, 0.4, 0.6, 0.8, and 1.0 m/s. Different curves with the same color represent various lateral velocities. The blue curves are the NSC of coefficients about *u*|*v*| and *u*|*w*|. The red curves are the NSC of coefficients about *uv* and *uw*.

The NSCs of coupling moment coefficients are shown in Figure 20. The sensitivity of coupling roll moment coefficients decreases with increasing lateral speed when the longitudinal velocity is larger than 0.4 m/s. The sensitive effect of longitudinal velocity on those coefficients reduces if the lateral speed increases. The sensitivity of M_{uw} and $M_{u|w|}$ show similar trend as roll moments only when the ROV move to its starboard. The sensitivity of yaw moment coefficients also decreases at larger lateral speeds but the motion direction is contrary to pitch moments. The sensitivity of roll and yaw moment coefficients about *uv* and *uw* is greater than that about *u*|*v*| and *u*|*w*|. Conversely, the sensitivity of $M_{u|v|}$ is greater than M_{uv}. The NSCs difference between M_{uw} and $M_{u|w|}$ is less than 8% when the longitudinal velocity and lateral velocity are 0.6 m/s and 0.03 m/s respectively.

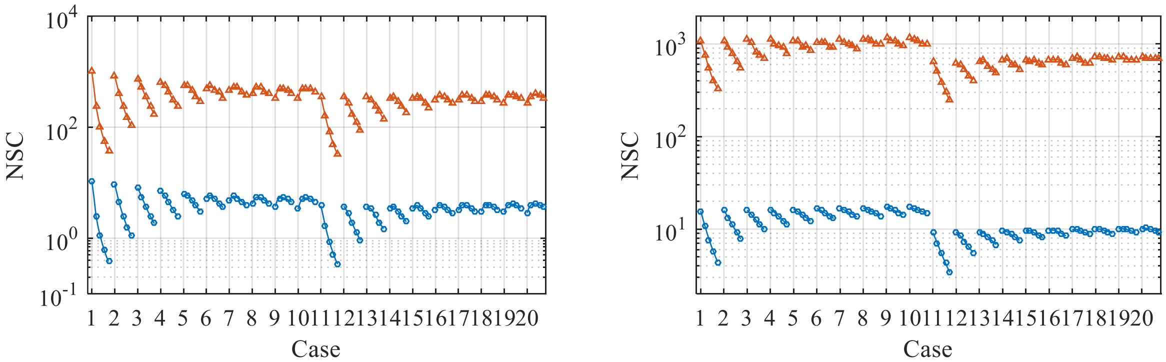

(a) The NSC of *Kuv* and *Ku*|*v*| (b) The NSC of *Kuw* and *Ku*|*w*|

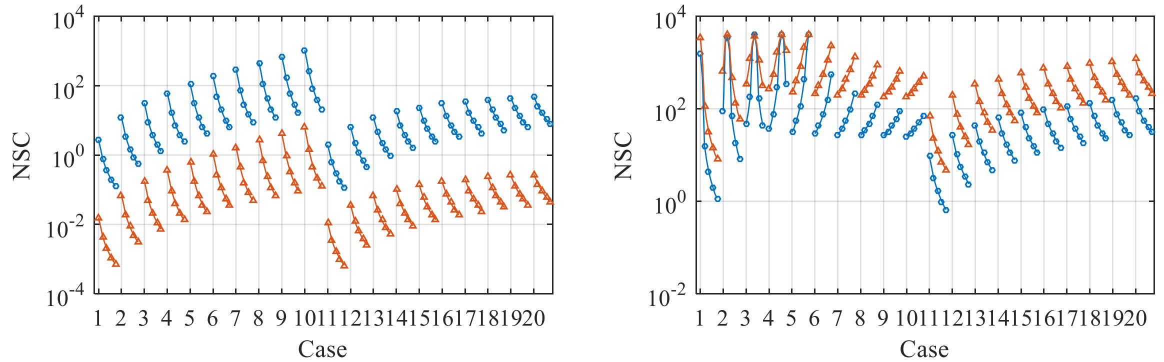

(c) The NSC of *Muv* and *Mu*|*v*| (d) The NSC of *Muw* and *Mu*|*w*|

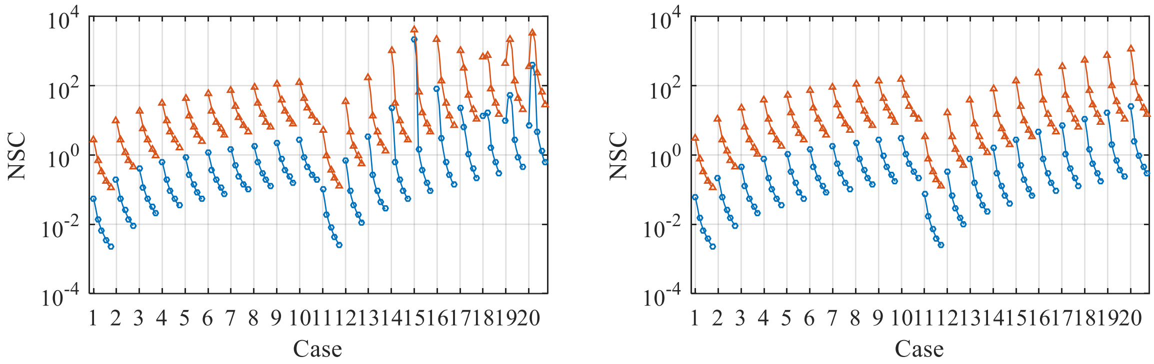

(e) The NSC of *Nuv* and *Nu*|*v*| (f) The NSC of *Nuw* and *Nu*|*w*|

Figure 20. The NSCs of coupling moment coefficients against the velocity in drift motion. The meaning of the color and sambal are the same as the Figure 19.

5.3. Stationary random motion

The stationary random motions were used to distinguish the sensitivity of 36 inertial hydrodynamic coefficients. The reason why we chose stationary random motions is that the acceleration must coexist with velocities which may influence the NSC of the inertial hydrodynamic coefficients because of the different growth rates of inertia and viscous load against acceleration and velocities. In these motions, the ROV moves as a stationary random process. And there are both accelerations and velocities. The trajectories are set to ensure the average velocity is zero which means the mean viscous loads are about zero and the influence of the viscous loads is minimized. The time series and power spectrum of the trajectories with different spectral peak frequencies (ω_p) are shown in Figure 21 where peak frequencies from ω_{p1} to ω_{p6} are 1.756, 1.273, 1.074, 0.905, 0.644, and 0.445 rad/s respectively. The details of the spectrums we used are discussed in section 6.

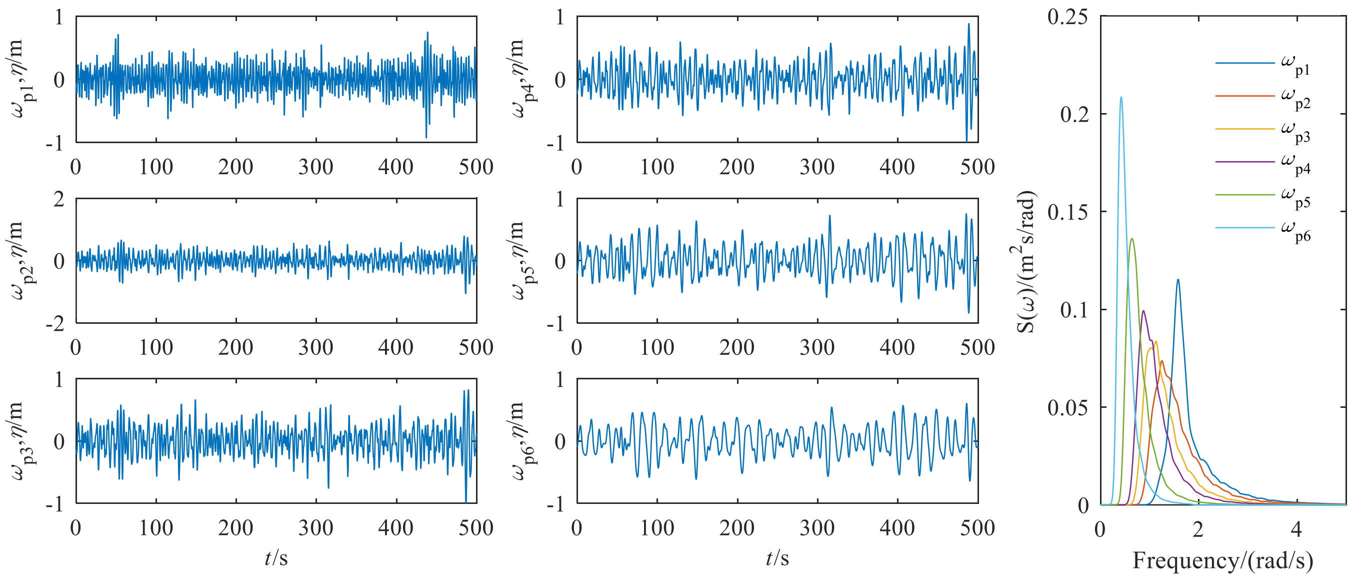

Figure 21. The times series and the power spectrum of trajectories.

The motion period effect on NSCs on inertial hydrodynamic coefficients is shown in Figure 22. The significant acceleration was calculated by the spectral peak frequency ω_p and the gravitational acceleration g. The motion period affects the $Z_{\dot{u}}$, $Z_{\dot{r}}$, $K_{\dot{r}}$, and $M_{\dot{v}}$ significantly. The relative sensitivity of the inertial hydrodynamic coefficients is consistent except $Z_{\dot{u}}$ and $Z_{\dot{r}}$. For example, Figure 22(b) can be explained that there is an order of the sensitivity of coefficients, $Y_{\dot{p}} > Y_{\dot{r}} > Y_{\dot{w}} > Y_{\dot{v}} > Y_{\dot{u}}$. Then we found that the sensitivity of the coefficients on the main diagonal of the matrix is not the largest in their DOF. The inertial hydrodynamic coefficients which are symmetry about the main diagonal do not have the same impact on the hydrodynamic loads in their DOF either.

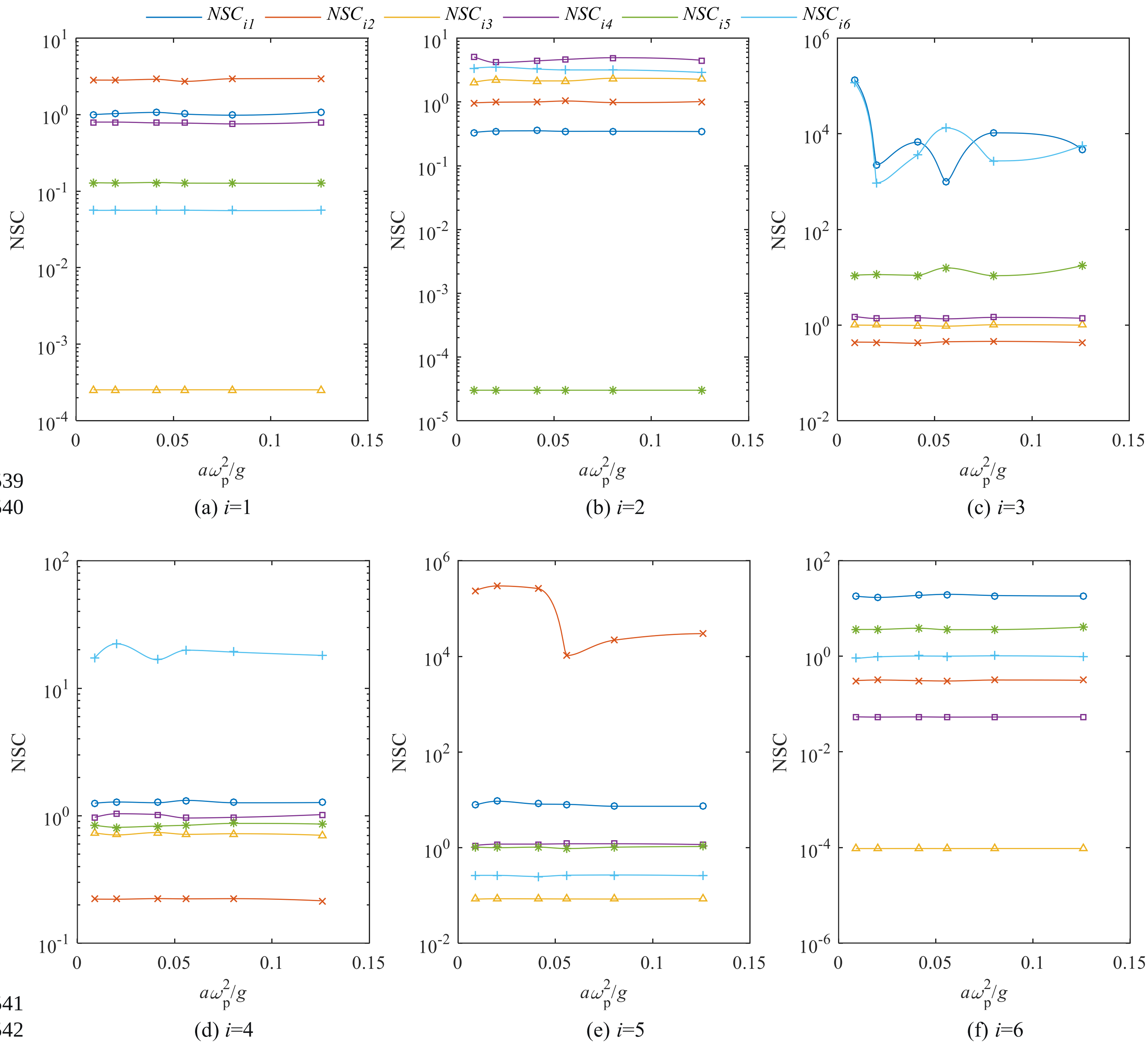

Figure 22. The NSCs of the inertial hydrodynamic coefficients, where NSC$_{i1\sim6}$ means the NSC of the inertial coefficients in *i* row, 1~6 columnin of eq. 3. Such as NSC$_{22}$ is the NSC of $X'_{\dot{v}}$, NSC$_{43}$ is the NSC of $K'_{\dot{w}}$, and NSC$_{51}$ is the NSC of $M_{\dot{u}}$.

5.4. Model simplification

The mathematical model can be simplified using sensitivity results. The NSC shows the importance of coefficients so the parameters with larger values for each group will be retained. Different coefficients can compare the sensitivity according to NSC because it is a nondimensional value. All cases with different speeds and frequencies will be used to simplify the model. The standard of simplifying is as follows: The coefficients whose NSC is less than a threshold value κ will be discarded; the NSC of the discarded coefficients should remain lower than κ for all cases. The simplified Models 1 and 2 can be expressed as follows.

- $\kappa = 0.1$, Model 1

Inertia loads

$$\boldsymbol{F_{MA}} = \begin{bmatrix} 1/2\rho L^3(X'_{\dot{u}}\dot{u} + X'_{\dot{v}}\dot{v} + LX'_{\dot{p}}\dot{p} + LX'_{\dot{q}}\dot{q}) \\ 1/2\rho L^3(Y'_{\dot{u}}\dot{u} + Y'_{\dot{v}}\dot{v} + Y'_{\dot{w}}\dot{w} + LY'_{\dot{p}}\dot{p} + LY'_{\dot{r}}\dot{r}) \\ 1/2\rho L^3(Z'_{\dot{u}}\dot{u} + Z'_{\dot{v}}\dot{v} + Z'_{\dot{w}}\dot{w} + LZ'_{\dot{p}}\dot{p} + LZ'_{\dot{q}}\dot{q} + LZ'_{\dot{r}}\dot{r}) \\ 1/2\rho L^4(K'_{\dot{u}}\dot{u} + K'_{\dot{v}}\dot{v} + K'_{\dot{w}}\dot{w} + LK'_{\dot{p}}\dot{p} + LK'_{\dot{q}}\dot{q} + LK'_{\dot{r}}\dot{r}) \\ 1/2\rho L^4(M_{\dot{u}}\dot{u} + M_{\dot{v}}\dot{v} + LM'_{\dot{p}}\dot{p} + LM'_{\dot{q}}\dot{q} + LM'_{\dot{r}}\dot{r}) \\ 1/2\rho L^4(N'_{\dot{u}}\dot{u} + N'_{\dot{v}}\dot{v} + LN'_{\dot{q}}\dot{q} + LN'_{\dot{r}}\dot{r}) \end{bmatrix} \tag{8}$$

Viscous loads related to uncoupled velocities

$$\boldsymbol{F_{UC}} = \{X_{UC} \quad Y_{UC} \quad Z_{UC} \quad K_{UC} \quad M_{UC} \quad N_{UC}\}^T \tag{9}$$

where,

$$X_{UC}\Big/ 1/2\rho L^2 = X'_{u|u|}u|u| + X'_{v|v|}v|v| + X'_{vv}v^2 + X'_{w|w|}w|w| + X'_{ww}w^2 + \sqrt{gl}(X'_{|w|}|w| + X'_w w + X'_p p + X'_q q + X'_r r)$$

$$Y_{UC}\Big/ 1/2\rho L^2 = Y'_{u|u|}u|u| + Y'_{uu}u^2 + Y'_{v|v|}v|v| + Y'_{ww}w^2 + \sqrt{gl}(Y'_{|u|}|u| + Y'_u u + Y'_{|w|}|w| + Y'_w w + Y'_p p + Y'_q q + Y'_r r)$$

$$Z_{UC}\Big/ 1/2\rho L^2 = Z'_{u|u|}u|u| + Z'_{uu}u^2 + Z'_{v|v|}v|v| + Z'_{vv}v^2 + Z'_{w|w|}w|w| + \sqrt{gl}(Z'_u u + Z'_v v + Z'_w w + Z'_p p + Z'_q q + Z'_r r)$$

$$K_{UC}\Big/ 1/2\rho L^3 = K'_{u|u|}u|u| + K'_{uu}u^2 + K'_{v|v|}v|v| + K'_{vv}v^2 + K'_{w|w|}w|w| + K'_{ww}w^2 + \sqrt{gl}(K'_{|u|}|u| + K'_u u + K'_{|v|}|v| + K'_v v + K'_{|w|}|w| + K'_w w + K'_p p + K'_q q + K'_r r)$$

$$M_{UC}\Big/ 1/2\rho L^3 = M'_{uu}u^2 + M'_{v|v|}v|v| + M'_{vv}v^2 + M'_{ww}w^2 + \sqrt{gl}(M'_{|u|}|u| + M'_u u + M'_{|v|}|v| + M'_v v + M'_p p + M'_q q + M'_r r)$$

$$N_{UC}\Big/ 1/2\rho L^3 = N'_{u|u|}u|u| + N'_{uu}u^2 + N'_{v|v|}v|v| + N'_{w|w|}w|w| + N'_{ww}w^2 + \sqrt{gl}(N'_u u + N'_v v + N'_w w + N'_p p + N'_q q + N'_r r)$$

- $\kappa = 0.01$, Model 2

Inertia loads

$$\boldsymbol{F_{MA}} = \begin{bmatrix} 1/2\rho L^3(X'_{\dot{u}}\dot{u} + X'_{\dot{v}}\dot{v} + LX'_{\dot{p}}\dot{p} + LX'_{\dot{q}}\dot{q} + LX'_{\dot{r}}\dot{r}) \\ 1/2\rho L^3(Y'_{\dot{u}}\dot{u} + Y'_{\dot{v}}\dot{v} + Y'_{\dot{w}}\dot{w} + LY'_{\dot{p}}\dot{p} + LY'_{\dot{r}}\dot{r}) \\ 1/2\rho L^3(Z'_{\dot{u}}\dot{u} + Z'_{\dot{v}}\dot{v} + Z'_{\dot{w}}\dot{w} + LZ'_{\dot{p}}\dot{p} + LZ'_{\dot{q}}\dot{q} + LZ'_{\dot{r}}\dot{r}) \\ 1/2\rho L^4(K'_{\dot{u}}\dot{u} + K'_{\dot{v}}\dot{v} + K'_{\dot{w}}\dot{w} + LK'_{\dot{p}}\dot{p} + LK'_{\dot{q}}\dot{q} + LK'_{\dot{r}}\dot{r}) \\ 1/2\rho L^4(M_{\dot{u}}\dot{u} + M_{\dot{v}}\dot{v} + M'_{\dot{w}}\dot{w} + LM'_{\dot{p}}\dot{p} + LM'_{\dot{q}}\dot{q} + LM'_{\dot{r}}\dot{r}) \\ 1/2\rho L^4(N'_{\dot{u}}\dot{u} + N'_{\dot{v}}\dot{v} + LN'_{\dot{p}}\dot{p} + LN'_{\dot{q}}\dot{q} + LN'_{\dot{r}}\dot{r}) \end{bmatrix} \tag{10}$$

Viscous loads related to uncoupled velocities

$$\boldsymbol{F_{UC}} = \{X_{UC} \quad Y_{UC} \quad Z_{UC} \quad K_{UC} \quad M_{UC} \quad N_{UC}\}^T \tag{11}$$

where,

$$X_{UC}\Big/ 1/2\rho L^2 = X'_{u|u|}u|u| + X'_{v|v|}v|v| + X'_{vv}v^2 + X'_{w|w|}w|w| + X'_{ww}w^2 + \sqrt{gl}(X'_{|v|}|v| + X'_v v + X'_{|w|}|w| + X'_w w + X'_p p + X'_q q + X'_r r)$$

$$Y_{UC}\Big/ 1/2\rho L^2 = Y'_{u|u|}u|u| + Y'_{uu}u^2 + Y'_{v|v|}v|v| + Y'_{w|w|}w|w| + Y'_{ww}w^2 + \sqrt{gl}(Y'_{|u|}|u| + Y'_u u + Y'_{|w|}|w| + Y'_w w + Y'_p p + Y'_q q + Y'_r r)$$

$$Z_{UC}\Big/ 1/2\rho L^2 = Z'_{u|u|}u|u| + Z'_{uu}u^2 + Z'_{v|v|}v|v| + Z'_{vv}v^2 + Z'_{w|w|}w|w| + \sqrt{gl}(Z'_u u + Z'_v v + Z'_w w + Z'_p p + Z'_q q + Z'_r r)$$

$$K_{UC}\Big/ 1/2\rho L^3 = K'_{u|u|}u|u| + K'_{uu}u^2 + K'_{v|v|}v|v| + K'_{vv}v^2 + K'_{w|w|}w|w| + K'_{ww}w^2 + \sqrt{gl}(K'_{|u|}|u| + K'_u u + K'_{|v|}|v| + K'_v v + K'_{|w|}|w| + K'_w w + K'_p p + K'_q q + K'_r r)$$

$$M_{UC}\Big/ 1/2\rho L^3 = M'_{u|u|}u|u| + M'_{uu}u^2 + M'_{v|v|}v|v| + M'_{vv}v^2 + M'_{w|w|}w|w| + M'_{ww}w^2 + \sqrt{gl}(M'_{|u|}|u| + M'_u u + M'_{|v|}|v| + M'_v v + M'_p p + M'_q q + M'_r r)$$

$$N_{UC}\Big/ 1/2\rho L^3 = N'_{u|u|}u|u| + N'_{uu}u^2 + N'_{v|v|}v|v| + N'_{w|w|}w|w| + N'_{ww}w^2 + \sqrt{gl}(N'_{|u|}|u| + N'_u u + N'_v v + N'_w w + N'_p p + N'_q q + N'_r r)$$

The motion simulation results based on the original model in section 2 and the simplified equations (9)-(12) in real scale are shown in Figure 23. The definition of screw-pitch 1 and 2 are shown in Figure 23(a). compares the roll, pitch, and yaw angle of three models. The initial longitudinal velocity is 1 m/s. The ROV starts at the origin of the space-fixed coordinate system and heads on the axis $+Ox_0$. The thrust force and moment in Gx0 and Gz0 of the body-fixed coordinate system are 320 N and 512 Nm. The initial longitudinal velocity is 0.8 m/s. The reason why those thrusts are chosen is that the ROV will do a nearly steady rotational motion and it is convenient to analyze the effect of different models. The ROV rotates to the starboard and rises.

The parameters of the rotational motion for the three models are shown in Table 4. There are more consistency between the original model and model 2. Compared to Model 1, Model 2 added a more linear longitudinal hydrodynamic coefficient about the lateral velocity and the lateral hydrodynamic coefficients about vertical the velocity. Therefore, the relative errors of horizontal motion calculated from Model 2 are smaller and the estimation of vertical position is better. However, the advantage of predicting the horizontal positions for Model 2 is not obvious.

Figure 24 shows the angles of three model calculations. The greatest relative errors of the average roll and pitch angle between Model 1 and the original model are over 15%. The results of the roll, pitch, and yaw angle that Model 2 predicates are closer to the original models of which the largest error is less than 1 %. The simulation results of the original model and Model 2 agree with each other. Though some discrepancies between the original model and Model 1 are smaller than 5%, the threshold value of NSC for 0.01 can also be considered for a more simple model.

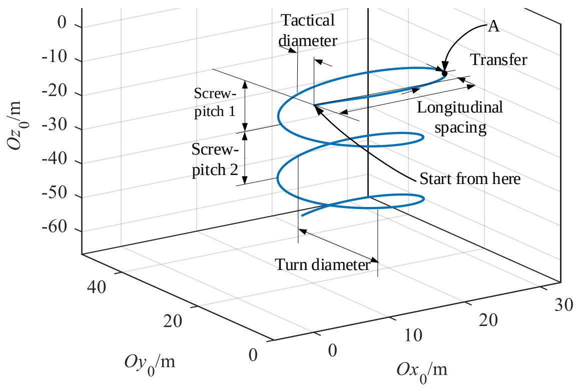

(a)

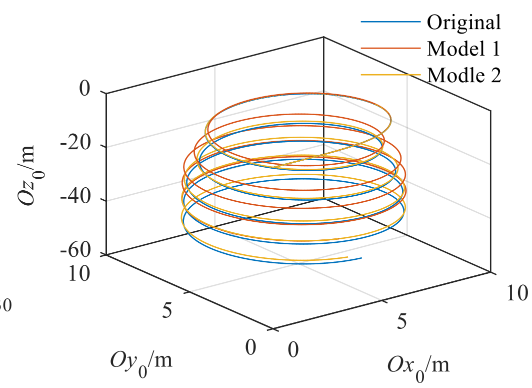

(b)

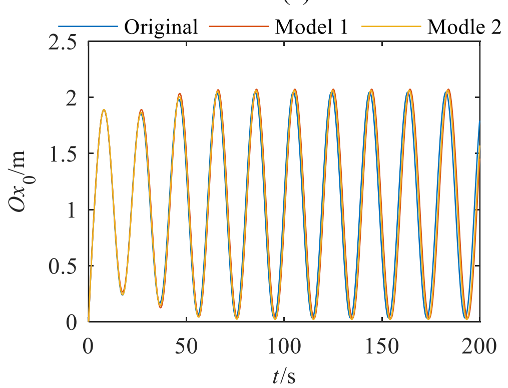

(c)

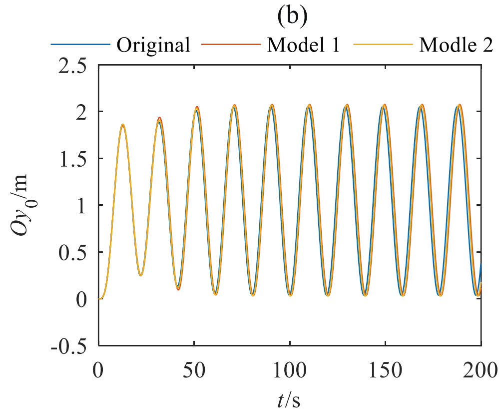

(d)

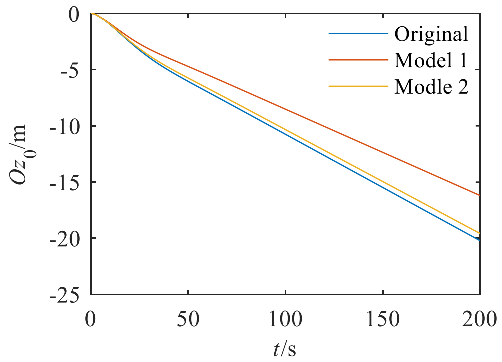

(e)

Figure 23. The simulation results of the original model $\kappa = 0$, the simplified model with $\kappa = 0.1$, and the model with $\kappa = 0.01$. (a) is the definition of rotational motion parameters where the yaw angle is 90° at point A and (b) is the trajectory of the ROV. (c), (d), and (e) is the positions of the Ox_0, Oy_0, and Oz_0 axis.

Table 4. The parameters of the rotational motions

	original model	Model 1		Model 2	
	/m	/m	error/%	/m	error/%
Longitudinal spacing	6.292	6.304	0.19	6.284	0.13
Transfer	1.259	1.272	1.08	1.250	0.67
Tactical diameter	7.461	7.402	0.79	7.467	0.09
Turn diameter	6.477	6.397	1.23	6.480	0.05
Screw-pitch 1	8.468	7.384	12.80	8.284	2.17
Screw-pitch 2	10.208	7.512	26.41	9.576	6.19

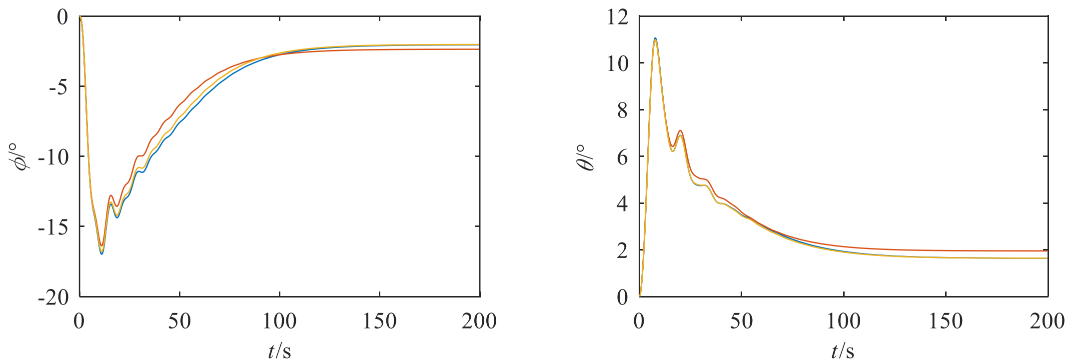

(a) (b)

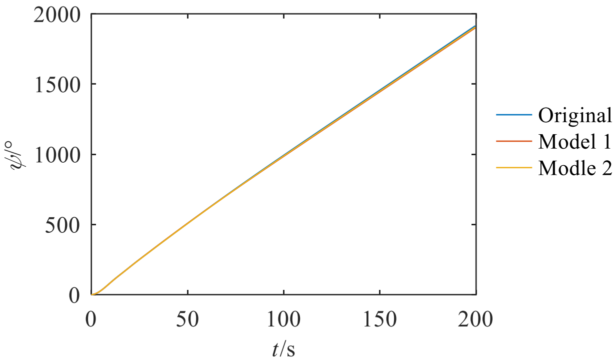

(c)

Figure 24. The simulation results of the original model, the Model 1 with $\kappa = 0.1$, and Model 2 with $\kappa = 0.01$. (a) is the roll angles, (b) is the pitch angles, and (c) is the yaw angles.

The results of zigzag-like motion simulations are plotted in Figure 25. The initial conditions are the same as the rotational motion simulations, but the yaw moment changes from 512 Nm to −512 Nm when the yaw angle reaches 10°. The yaw moment changes 512 Nm again when the yaw moment is −10°. The trajectories of the ROV do not show a significant starboard drift with a set of yaw motions. The periodically changing moment brings the accelerations and velocities of lateral and yaw motions which induce motions in other DOFs because the viscous hydrodynamic loads are related to the velocities in 6DOFs and the inertial coefficient constitutes a 6×6 matrix that affects all the accelerations in 6DOFs. Under the action of the coupling model, the vertical trajectories also display the heave, pitch, and roll motion periodically.

The overshoot angles and course change lags are used to compare the effects of models. The moments that the peaks of rotational angles appear show larger differences after 20 seconds. The parameters of the zigzag-like motions are listed in Table 5. The errors of overshot angles are larger than the course change lags. The accuracy of Model 2 does show an obvious preponderance than Model 1.

The position of the ROV does not show peak values. Therefore, to compare the positions that the three models calculated in Figure 26(a), the linear relations between position coordinates (x_g, y_g, z_g) for the original model, (x_{g1}, y_{g1}, z_{g1}) for Model 1, and (x_{g2}, y_{g2}, z_{g2}) for Model 2 are shown in Figure 26(b). The meaning of S1 and S2 is the relation of the results from Model 1 and Model 2 to the original model. The positions are nondimensional by their maximum values. The more the slope of curves S1 and S2 closer to 1 the fewer effects of different models on motion. The relative errors of the slope of each curve for Models 1 and 2 are less than 8% and 3% respectively. All in all, model 2 could be an acceptable model for the ROV.

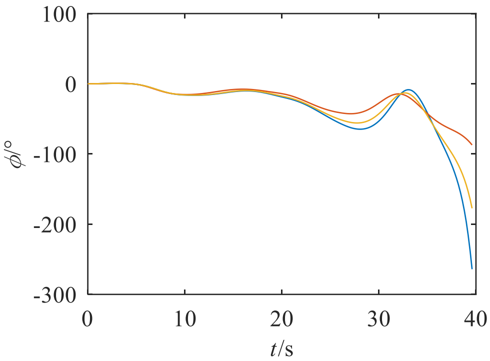

(a)

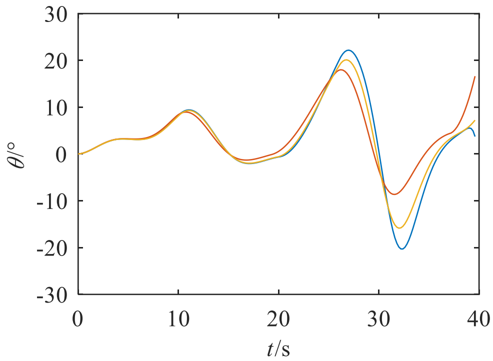

(b)

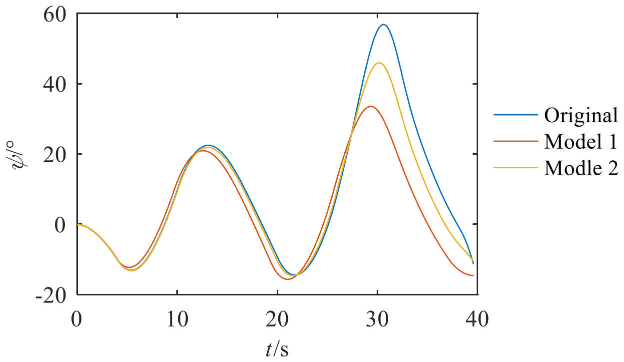

(c)

Figure 25. The results of zigzag-like motion simulations. (a) is the roll angles, (b) is the pitch angles, and (c) is the yaw angles.

Table 5-1. The overshot angles of the zigzag-like motions

	original model	Model 1		Model 2	
	/°	/°	error/%	/°	/%
1st Overshot angle	−3.12	−2.29	−26.60	−3.21	2.88
2nd Overshot angle	12.46	11.85	−4.90	10.91	−12.44
3rd Overshot angle	−4.47	−5.69	27.29	−4.64	3.80
4th Overshot angle	46.85	23.51	−49.82	35.95	−23.27

Table 6-2. The course change lags of the zigzag-like motions

	original model/s	Model 1/s	Model 2/s
1st Course change lag	1.41	1.2	1.41
2nd Course change lag	3.2	2.11	3
3rd Course change lag	1.8	1.8	1.8
4th Course change lag	4.6	3.8	4.2

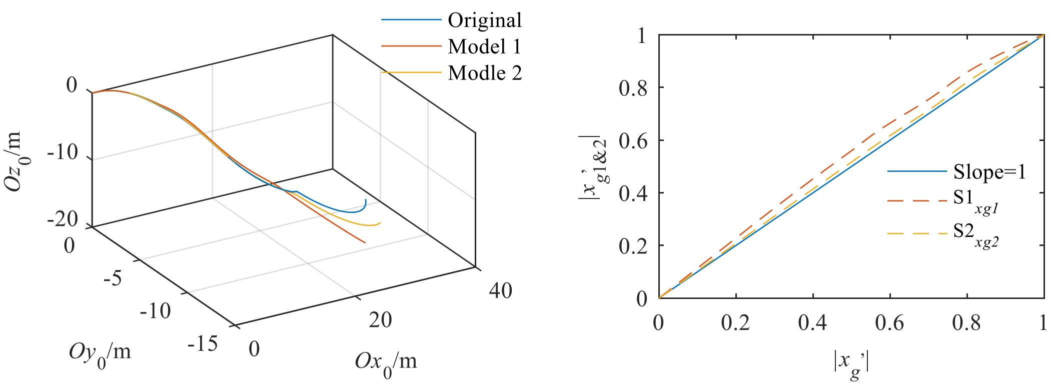

(a) The trajectory (b) Ox_0 position

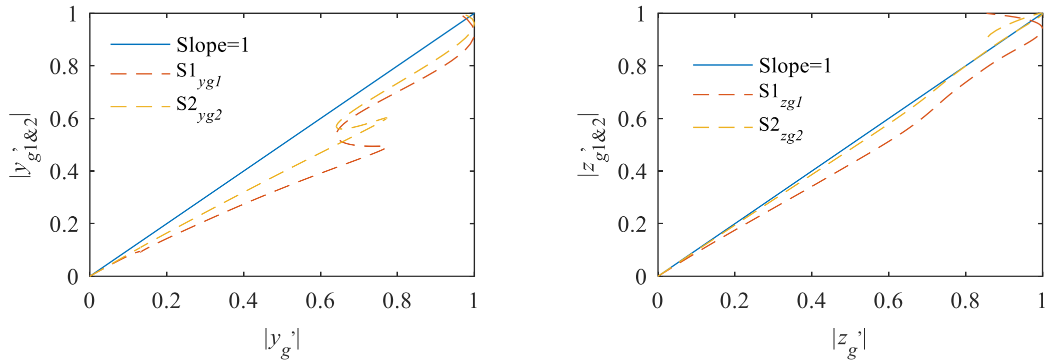

(a) Oy_0 position (b) Oz_0 position

Figure 26. The positions form the original model, Model 1, and Model 2.

6. Discussion

The above chapters carried out the key results to achieve our main goal that estimating the hydrodynamic coefficients and simplifying the mathematical model. In this section, we will analyze and discuss other results of the experiments and simulations.

The hydrodynamic loads on an open-frame ROV represent significant nonlinear and asymmetrical characteristics. Due to the complex shape of the ROV model, the velocity in one DOF affects all the hydrodynamic forces and moments in 6DOFs. The hydrodynamic loads in the same DOF and velocity but in opposite directions are different. The discrepancy increases with the drag speed. The largest relative difference appears at the lateral force in ±X cases, the longitudinal force in ±Y cases, and the roll moment in ±Z cases. The loads other than the main direction of motion show obvious nonlinear trends, especially for the hydrodynamic moments. It is proved that there are amount of nonnegligible second-order hydrodynamic coefficients from static tests. To describe the nonlinear and asymmetric hydrodynamic loads of the ROV model, we chose a quadratic absolute value function to fit the results. The main reason why we did not use the third-order model is that we thought the hydrodynamic loads should abide by the rule proportional to the square of the velocity. Another reason is that the hydrodynamic load should be monotonic with velocity, and there are hydrodynamic loads that are approximate to the even function. A typical difference between using the third-order model (f1) and the quadratic absolute value function (f2) to fit the lateral force results in longitudinal static tests is shown in Figure 27. There is good agreement between the curves and raw data in the range of speeds in tests though, the third-order model shows a significant non-monotonic when the velocity is larger than the maximum speed we tested because of the inherent attribute of the third-order model. Of course, the speed of a vehicle should be in the range of the test conditions, but it still means the slope of the curve for the speed we tested may be wrong.

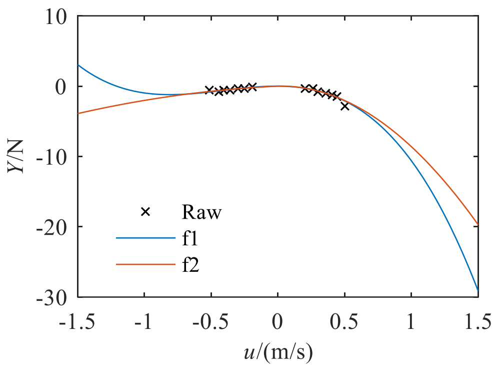

Figure 27. The comparison of the third-order model (f1) and the quadratic absolute value function (f2).

There is still a flaw in the quadratic absolute value function: the hydrodynamic model is continuous but not differentiable when the speed is zero. We thought that it did not affect the use of the quadratic absolute value function because the differential of force does mean anything in a steady motion simulation. May the differentiable model in zero speed should be considered if the motion speed and the response of a vehicle are high. There are a few characteristics of the model based on the quadratic absolute value function. The coefficients' order and whether there is an absolute value of velocity follow the rules of hydrodynamic loads against the static velocity. The second-order coefficient related to the absolute velocity is larger if the relation between hydrodynamic loads and the moving speed is close to an odd function. On the contrary, the second-order coefficient related to the velocity squared is larger if the relation between hydrodynamic loads and the moving speed is close to an even function. The difference between those two kind of coefficients show the asymmetrical of the hydrodynamic against the speeds.

The accelerometers were used to monitor the displacement and frequency. However, the data from accelerometers were not used to calculate the velocities for the dynamic tests because there will be errors for the integral based on discrete acceleration measurements. We only used accelerometers to calculate the amplitude and compared them to the parameters we inputted. The 6-DOF parallel platform moved gradually from static to the trajectories we needed. Therefore the time it started moving and became stable is important for coefficient estimating. Therefore, there was a second purpose for the accelerators that judge the phase of motions. For example, the raw vertical acceleration (Oy0 direction in the test) in heave tests of 0.3 Hz and its filtered curve is shown in Figure 28. The large acceleration peaks were caused by the mechanical shock when the 6-DOF parallel platform changed its moving direction. The 6-DOF parallel platform needed at least 25 seconds to meet a stable motion state and the measurements in the last period were affected by the sudden stop of the platform. Therefore, only the load data between 25 seconds and the last period were used. The average amplitude and frequency of acceleration in the valid range are 0.1001 m/s^2 and 0.3003 Hz which agree with the inputted parameters.

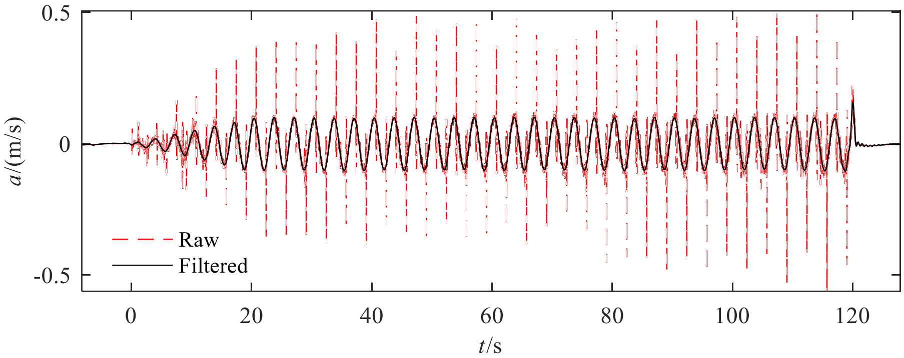

Figure 28. The acceleration in the heave test of 0.3 Hz.

In the PMM tests, all 36 inertial hydrodynamic coefficients were estimated. However, the added mass matrix is not symmetrical. A similar phenomenon was discovered in other ROV model tests [13]. There are also asymmetrical coefficients $Z_{\dot{p}}$ and $M_{\dot{w}}$ for the DARPA Suboff model and BB2 generic submarine [23, 29]. There is still a nonsymmetric matrix occurring in an AUV whose outline is simpler and more symmetrical [22]. From the physical standpoint, the inertial hydrodynamic loads represent the amount of fluid accelerated with the ROV. The cross-coupling coefficients such as $X_{\dot{v}}$, $Y_{\dot{w}}$, and $M_{\dot{w}}$ are nonzero for the ROV absence symmetry. The degrees for the particles of fluid adjacent to the ROV model, when it is accelerated, depend on their position relative to the body. There is a discrepancy between the inertial hydrodynamic loads in different directions caused by an acceleration in one DOF because the added mass is a weighted integration of this entire mass of fluid [48]. The accelerated particles of fluid for local structures may vary in various directions due to the viscosity effect on boundary layer separation and the mutual interference of local structures and also influence the global added mass.

The hydrodynamic loads in surge, sway, and heave PMM tests include inertial and drag terms. The drag loads calculated by subtracting the inertial hydrodynamic we estimated from the data measured from the PMM tests are compared to the values from the original model in Figure 29. It is indicated that the oscillation frequency has a significant impact on drag load in one period. The load that appears at the maximum velocity shows a definite offset to the results we calculated. The drag loads at the same velocity but different phases are also inequality. The main reason why the difference exists is the historical effect of hydrodynamics which is caused by the effect of discrepancy between the wake in an oscillation and drag motion. The longitudinal force in surge motion along the current direction, as a result, the longitudinal force for dynamic tests is smaller when the relative velocity approaches the maximum because of the underdevelopment wake influence by the motion in the last period. The longitudinal force is larger than the mathematical model results when the relative velocity reaches the minimum due to the undissipated large-strength vortex which is induced by the larger relative velocity in the last period. In the sway and heave tests, the historical effect even changes the direction of the drag forces. As the velocity decreases as the frequency, the historical effect fades into obscurity. However, the drag force shows fluctuation because of the slightly larger turbulence intensity and the shake of the strut at low frequency.

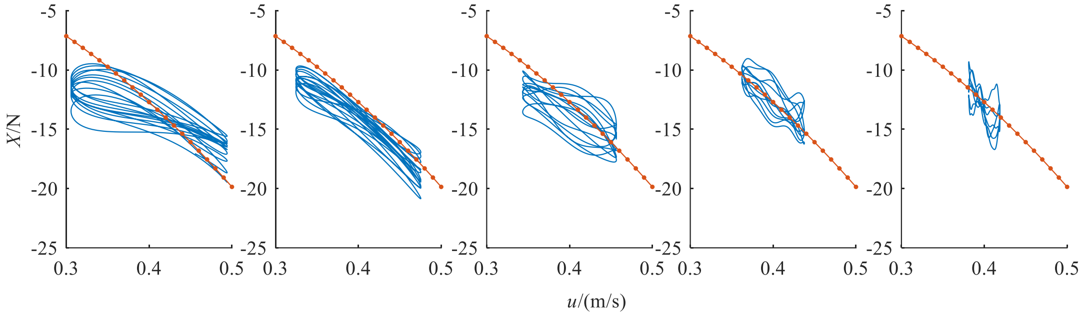

(a)

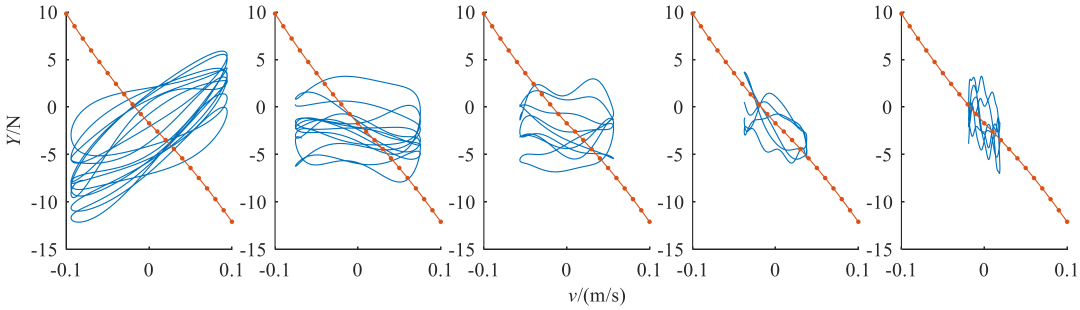

(b)

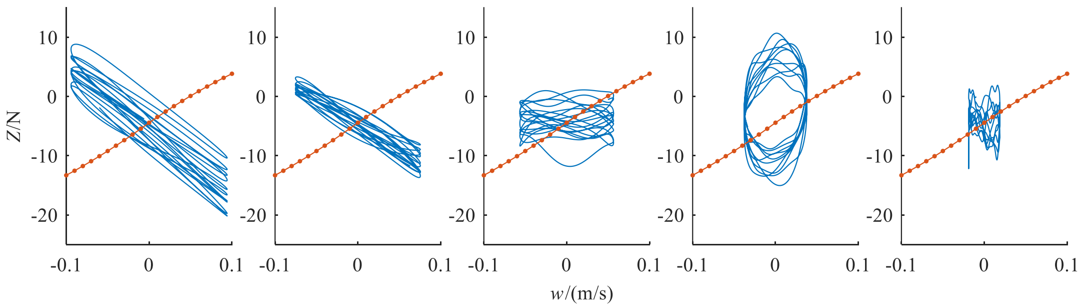

(c)

Figure 29. The viscous loads from PMM tests and the mathematical model against the oscillation velocity for the longitudinal force in surge tests (a), the lateral force in sway tests (b), and the vertical force in heave tests (c).

Both PMM tests and static tests can estimate the linear drag coefficients. The reason why we use the static test results to calculate the nonlinear and linear drag coefficients is that the historical effect influences the results significantly as we analyzed in Figure 29. Therefore, the static tests can obtain more accurate coefficients than PMM tests. However, there is an obvious shortcoming of the mathematical model we used that can not consider the historical effect. It will result in the untrue hydrodynamic and motion response of the ROV in an oscillation. To model the historical effect of the ROV, the unsteady load on the ROV will be studied in our next study about the impulse-response relation, and the new mathematical model will be compared with the original model herein.

The sensitivity of the hydrodynamic coefficients in 6DOF was investigated via the Normalized Sensitivity Coefficients (NSCs). NSC excludes the effect of the size of the coefficient value and the hydrodynamic load via non-dimensional. The main idea of the sensitivity analysis is to vary the speed and acceleration of the ROV model and then calculate the NSC of each coefficient. The NSC can be used to compare the coefficients in the same and different DOFs. There are only linear and angular velocities in the drag and drift motions, and the inertial hydrodynamic could be eliminated.

According to the NSC results in section 5, the hydrodynamic load, and the coefficients in section 4, the sensitivity of the hydrodynamic coefficients is not only affected by the size of the coefficient values but also by the character of the hydrodynamic loads and the motion velocity. If the hydrodynamic load is small, the variation of a coefficient induces a larger effect of the hyd-term relatives to that coefficient on the hydrodynamic load. For example, the longitudinal force against the lateral velocity raises as the nonlinear coefficients X_{vv} and $X_{v|v|}$ increase as shown in Figure 30(a) in which the linear coefficients remain unchanged. According to the definition of NSC, the NSCs for the velocity less and over zero are $\mathrm{NSC}\big|_{v<0}=\left|\dfrac{X_{vv}v^2}{-X_{v|v|}vv+X_{vv}v^2+X_{|v|}v+X_v v}\right|\Bigg|_{v<0}$ and $\mathrm{NSC}\big|_{v>0}=\left|\dfrac{X_{vv}v^2}{X_{v|v|}vv+X_{vv}v^2+X_{|v|}v+X_v v}\right|\Bigg|_{v>0}$ respectively where the denominators are the hydrodynamic loads. Because $X_{v|v|}$ and X_{vv} are greater than zero, the limitation of $\mathrm{NSC}\big|_{v<0}$ is larger than $\mathrm{NSC}\big|_{v>0}$ when the velocity approaches the infinity as shown in Figure 30(b). similar rules appear at the linear coefficients. The difference is the limitation for $v\to\pm\infty$ is zero due to the order of the denominators of NSC for linear coefficients being greater. The larger the nonlinear coefficients are the faster the NSCs close to the limitation of infinity and hence the sensitivity of the nonlinear coefficients is even bigger when the motion velocity is low and growing. The larger the linear coefficients are the NSCs close to the limitation of zero speed and the sensitivity of the linear coefficients is even smaller when the motion velocity is low and descending.

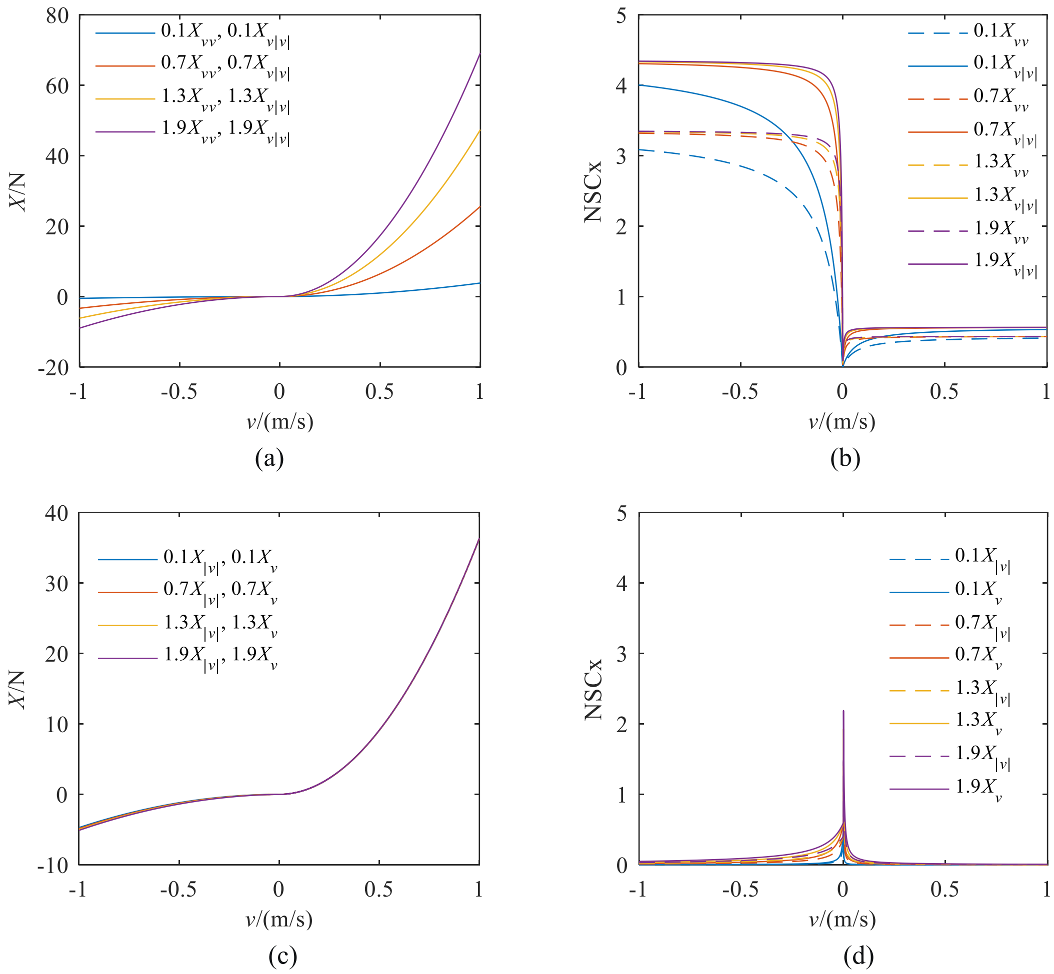

Figure 30. The NSC variation against hydrodynamic coefficients. The viscous hydrodynamic load (a)(c) of four group coefficients and the NSC of eight coefficients (b)(d).

To avoid the effect of the velocity, random motions were used. To be honest, the spectrums of the random motion come from the JONSWAP wave spectrum with three key parameters including spectral peak period and significant wave height [49]. The spectral periods were chosen according to the wave period-height distribution [50]. The significant wave height of 1 m was used because it is a typical operating limit for an offshore operation. The wave spectral period is the motion peak period of the ROV model and the significant wave height indicates the motion amplitude. The reason why we used the wave spectrum is that it is difficult to determine the motion period in a real ROV underwater operation, while the wave effect on ROV can be estimated. It is significant to study the NSC referring to the wave spectrum because the wave-induced vessel motion is a critical affecter on the dynamic response of an ROV in launching operation [51-53]. The control system still needs to resist the tension variation of the umbilical cable which comes from the wave-induced vessel motion [54, 55].

In this paper, we did not design a control system for the ROV, which caused a set of easily influenced irregular trajectories. On this basis, 0.01 was chosen as the threshold value used to filter the coefficients via NSC based on the free-running tests. However, the threshold value could be changed for other kinds of ROV. It could be better to increase the threshold value when the mathematical model is used for a model-based control system. We may use different retention methods in the future in line with the actual use motions.

7. Conclusion

The paper presents the results of an experimental investigation and mathematical model simplification of a work-class ROV model, which was held with a 6-DOF parallel platform. The experiment includes the drag and PMM tests which enable the investigation of viscous and inertial hydrodynamic loads and coefficients respectively.

The viscous force and moments relative to one kind of velocity in each three translation DOFs were measured in longitudinal, lateral, and vertical drag tests. The first finding was that there were all six DOF hydrodynamic loads on the ROV when it moved in one DOF. The moving direction has a significant impact on the hydrodynamic loads. The drift and trim drag tests are performed to estimate the velocity coupling hydrodynamic loads. The linear and nonlinear coefficients were estimated by fitting a quadratic absolute value function with the results from the drag tests. The small amplitude PMM tests in the 6-DOF including the roll, pure pitch, and pure yaw motions were carried out. The historical loops were used to analyze the relationship between the inertial and viscous hydrodynamic loads. We found that the inertial and viscous load increase with oscillation frequency and the asymmetrical hydrodynamics induce non-centrosymmetric loops, especially for the longitudinal force and pitch moment in surge motion, the roll moment in roll motion, and the longitudinal force in pure yaw motion. All 36 inertial hydrodynamic coefficients and linear angular velocity hydrodynamic derivatives were estimated. The inertial and viscous terms of the hydrodynamic load at the oscillation frequency showed linear variation with acceleration. The exception is the viscous term of roll moment appeared nonlinear phenomenon.

The Normalized Sensitivity Coefficient (NSC) was defined to evaluate the sensitivity of hydrodynamic coefficients on the ROV in 6-DOF motion based on the mathematical model established via the model tests. By using a series of velocities in one DOF and calculating the NSCs, the sensitivity of the viscous hydrodynamic coefficients could be compared. To avoid the velocity effect, the stationary random motions were used to analyze the sensitivity of the inertial hydrodynamic coefficients. The results of NSC showed that the size of the coefficient, the character of the hydrodynamic loads, and the motion velocity are both the key factors that affect the sensitivity of the viscous hydrodynamic coefficients. The linear coefficients may have an approximate value to the larger nonlinear coefficients in some cases. The acceleration indeed affects the inertial hydrodynamic coefficients, but the relative strength of the sensitivity did not change between coefficients in the same DOF. The mathematical model was simplified and it was verified by the rotational and overshot motions. Results illustrate that the threshold value we chose and the simplified model was suitable for the ROV. This knowledge of the sensitivity of the mathematical mode will be important when the present model is used as a testbed for other vehicles.

Acknowledgements

Author contributions

Ruinan Guo: Writing- Original Draft, Formal analysis. **Yingfei Zan**: Writing- Reviewing & Editing, Methodology. **Xiaofang Luo**: Writing- Reviewing and Data Curation. **Xiandong Ma**: Investigation, Conceptualization. **Duanfeng Han**: Data Curation. **Xu Bai**: Visualization.

Reference

[1] Elvander J, Hawkes G. ROVs and AUVs in Support of Marine Renewable Technologies. Oceans. Hampton Roads, VA, USA2012. p. 1-6.

[2] Sarkar A, Gudmestad OT. Study on a new method for installing a monopile and a fully integrated offshore wind turbine structure. Marine Structures. 2013;33:160-87.

[3] Lieng JT, Sturm H, Hasselø KK. Dynamically installed anchors for floating offshore wind turbines. Ocean Engineering. 2022;266.

[4] Myhr A, Bjerkseter C, Ågotnes A, Nygaard TA. Levelised cost of energy for offshore floating wind turbines in a life cycle perspective. Renewable Energy. 2014;66:714-28.

[5] Barlow E, Tezcaner Öztürk D, Revie M, Boulougouris E, Day AH, Akartunalı K. Exploring the impact of innovative developments to the installation process for an offshore wind farm. Ocean Engineering. 2015;109:623-34.

[6] Trslić P, Rossi M, Sivčev S, Dooly G, Coleman J, Omerdić E, et al. Long term, inspection class ROV deployment approach for remote monitoring and inspection. OCEANS 2018 MTS/IEEE Charleston. Charleston, SC, USA: IEEE; 2018. p. 1-6.

[7] Chung WC, Pestana GR, Kim M. Structural health monitoring for TLP-FOWT (floating offshore wind turbine) tendon using sensors. Applied Ocean Research. 2021;113.

[8] ter Hofstede R, Driessen FMF, Elzinga PJ, Van Koningsveld M, Schutter M. Offshore wind farms contribute to epibenthic biodiversity in the North Sea. Journal of Sea Research. 2022;185.

[9] Liu Y, Hajj M, Bao Y. Review of robot-based damage assessment for offshore wind turbines. Renewable and Sustainable Energy Reviews. 2022;158.

[10] Sivčev S, Omerdić E, Dooly G, Coleman J, Toal D. Towards Inspection of Marine Energy Devices Using ROVs: Floating Wind Turbine Motion Replication. Third Iberian Robotics Conference. Sanya, China: Springer; 2017.

[11] Santos P, Santos M, Trslic P, Weir A, Dooly G, Omerdic E, et al. Developments in Underwater Robot Capabilities for Offshore Wind. OCEANS 2023 - Limerick. Limerick, Ireland: IEEE; 2023. p. 1-5.

[12] Fossen. TI. Handbook of marine craft hydrodynamics and motion control. Second Edition ed. Trondheim, Norway: Wiley; 2021.

[13] Xu SJ, Ma QW, Han DF. Experimental study on inertial hydrodynamic behaviors of a complex remotely operated vehicle. European Journal of Mechanics - B/Fluids. 2017;65.

[14] Xu SJ, Han DF, Ma QW. Hydrodynamic forces and moments acting on a remotely operate vehicle with an asymmetric shape moving in a vertical plane. European Journal of Mechanics - B/Fluids. 2015;54:1-9.

[15] Fan S, Lian L, Ren P, Huang G. Oblique Towing Test and Maneuver Simulation at Low Speed and Large Drift Angle for Deep Sea Open-Framed Remotely Operated Vehicle. Journal of Hydrodynamics. 2012;24:280-6.

[16] Ahmed F, Xiang X, Jiang C, Xiang G, Yang S. Survey on traditional and AI based estimation techniques for hydrodynamic coefficients of autonomous underwater vehicle. Ocean Engineering. 2023;268.

[17] Lee S-K, Joung T-H, Cheon S-J, Jang T-S, Lee J-H. Evaluation of the added mass for a spheroid-type unmanned underwater vehicle by vertical planar motion mechanism test. International Journal of Naval Architecture and Ocean Engineering. 2011;3:174-80.

[18] Jung J-W, Jeong J-H, Kim I-G, Lee S-K. Experimental Study on Hydrodynamic Coefficients of Autonomous Underwater Glider Using Vertical Planar Motion Mechanism Test. Journal of Ocean Engineering and Technology. 2014;28:119-25.

[19] Jung J-W, Jeong J-H, Kim I-G, Lee S-K. Estimation of Hydrodynamic Derivatives of Submarine Model by Using VPMM Test. Journal of Navigation and Port Research. 2014;38:97-103.

[20] Jeong J-H, Ok J-H, Lee C-S, Lee J-M, Lee S-K. Estimation of Hydrodynamic Derivatives and Dynamic Stability for Submarine Using Captive Model Test. Journal of Navigation and Port Research. 2015;39:173-8.

[21] Nouri NM, Mostafapour K, Bahadori R. An apparatus to estimate the hydrodynamic coefficients of autonomous underwater vehicles using water tunnel testing. Rev Sci Instrum. 2016;87:065106.

[22] Park J, Rhee SH, Yoon HK, Lee S, Seo J. Effects of a propulsor on the maneuverability of an autonomous underwater vehicle in vertical planar motion mechanism tests. Applied Ocean Research. 2020;103.

[23] Kim D-H, Kim Y, Baek H-M, Choi Y-M, Kim YJ, Park H, et al. Experimental study of the hydrodynamic maneuvering coefficients for a BB2 generic submarine using the planar motion mechanism. Ocean Engineering. 2023;271.

[24] Lin Y-H, Tseng S-H, Chen Y-H. The experimental study on maneuvering derivatives of a submerged body SUBOFF by implementing the Planar Motion Mechanism tests. Ocean Engineering. 2018;170:120-35.

[25] Lin Y-H, Chiu Y-C. The estimation of hydrodynamic coefficients of an autonomous underwater vehicle by comparing a dynamic mesh model with a horizontal planar motion mechanism experiment. Ocean Engineering. 2022;249.

[26] Saout O, Ananthakrishnan P. Hydrodynamic and dynamic analysis to determine the directional stability of an underwater vehicle near a free surface. Applied Ocean Research. 2011;33:158-67.

[27] Lee S, Choi H-S, Kim J-Y, Paik K-J. A numerical study on hydrodynamic maneuvering derivatives for heave-pitch coupling motion of a ray-type underwater glider. International Journal of Naval Architecture and Ocean Engineering. 2020;12:892-901.

[28] Fan S, Lian L, Ren P. Research on hydrodynamics model test for deepsea open-framed remotely operated vehicle. China Ocean Engineering. 2012;26:329-39.

[29] Liang X, Ma N, Liu H, Gu X. Experimental study on the maneuvering derivatives of a half-scale SUBOFF model in the vertical plane. Ocean Engineering. 2021;233.

[30] Lu Y, Wu J, Li W, Wu Y. A new six-dof parallel mechanism for captive model test. Polish Maritime Research 2020;27:4-15.

[31] Xu H, Hassani V, Guedes Soares C. Uncertainty analysis of the hydrodynamic coefficients estimation of a nonlinear manoeuvring model based on planar motion mechanism tests. Ocean Engineering. 2019;173:450-9.

[32] Xu H, Hassani V, Guedes Soares C. Truncated least square support vector machine for parameter estimation of a nonlinear manoeuvring model based on PMM tests. Applied Ocean Research. 2020;97.

[33] Vijayakumar R, Rayaprolu VSS. Sensitivity Analysis of the Turning Motion of an Underwater Glider on the Viscous Hydrodynamic Coefficients. Defence Science Journal. 2021;71:709-17.

[34] Yeo DJ, Rhee KP. Sensitivity analysis of submersibles' manoeuvrability and its application to the design of actuator inputs. Ocean Engineering. 2006;33:2270-86.

[35] Abolvafaie M, Koofigar HR, Malekzadeh M. CLASSIFICATION OF HYDRODYNAMIC COEFFICIENTS OF AUTONOMOUS UNDERWATER VEHICLES BASED ON SENSITIVITY ANALYSES IN STANDARD MANEUVERS. Journal of Marine Science and Technology. 2018;26:1-10.

[36] Sen D. A Study on Sensitivity of Maneuverability Performance on the Hydrodynamic Coefficients for Submerged Bodies. J Ship Res. 2000;44:186-96.

[37] Perrault D, Bose N, O'Young S, Williams CD. Sensitivity of AUV response to variations in hydrodynamic parameters. Ocean Engineering. 2003;30:779-811.

[38] Safari F, Rafeeyan M, Danesh M. Estimation of hydrodynamic coefficients and simplification of the depth model of an AUV using CFD and sensitivity analysis. Ocean Engineering. 2022;263.

[39] Jeon M, Tien Thua N, Hyeon Kyu Y, Hyeon Jin C. A Study on Verification of the Dynamic Modeling for a Submerged Body Based on Numerical Simulation. International Journal of Engineering and Technology Innovation. 2020;10:107-20.

[40] Ray A, Sen D, Singh S, Seshadri V. Quantification of uncertainty in manoeuvring characteristics for design of underwater vehicles. The International Journal of Maritime Engineering. 2010;152:A71-A84.

[41] Xu F, Zou Z-j, Yin J-c, Cao J. Parametric Identification and Sensitivity Analysis for Autonomous Underwater Vehicles in Diving Plane. Journal of Hydrodynamics. 2012;24:744-51.

[42] Wang D, Wang Y, Liu J, Hu Z, Zhang W, Wang Z, et al. An integrated dynamic modeling method for underwater vehicle with hull, propeller and rudder. Ocean Engineering. 2023;282.

[43] Perrault D, Bose N, O'Young S, Williams D. Sensitivity of AUV added mass coefficients to variations in hull and control plane geometry. Ocean Engineering 2003;23:645–71.

[44] Jeon M, Yoon HK, Hwang J, Cho HJ. Analysis of the dynamic characteristics for the change of design parameters of an underwater vehicle using sensitivity analysis. International Journal of Naval Architecture and Ocean Engineering. 2018;10:508-19.

[45] Guo R, Zan Y, Huang F, Han D, Li B. Investigating the free surface effect on the hydrodynamics of an rov moving along a straight path at design speed The ASME 2023 42nd International Conference on Ocean, Offshore and Arctic Engineering. Melbourne, Australia: ASME; 2023.

[46] Jamil MA, Imtiaz N, Ng KC, Xu BB, Yaqoob H, Sultan M, et al. Experimental and parametric sensitivity analysis of a novel indirect evaporative cooler for greener cooling. Thermal Science and Engineering Progress. 2023;42.

[47] Qureshi BA, Zubair SM. A comprehensive design and rating study of evaporative coolers and condensers. Part II. Sensitivity analysis. International Journal of Refrigeration. 2006;29:659-68.

[48] Newman JN. MarineHydrodynamics. 40th anniversary edition ed. Cambridge, MA: The MIT Pres; 2017.

[49] Chakrabarti S, Halkyard J, Capanoglu C. Handbook of offshore engineering. London: Elsevier; 2005.

[50] Wang X, Ying Z, Chen Z. The Analysis Of The Joint Limitation Condition Of Wave Height-Period On The Floating Crane Lifting Operation. Proceedings of the ASME 2019 38th International Conference on Ocean, Offshore and Arctic Engineering. Glasgow, Scotland, UK: ASME; 2019. p. 1-8.

[51] Landstad O, Halvorsen HS, Øveraas H, Smines V, Johansen TA. Dynamic positioning of ROV in the wave zone during launch and recovery from a small surface vessel. Ocean Engineering. 2021;235.

[52] Lubis MB, Kimiaei M. Wave flume and numerical test on launch and recovery of ultra-deep-water ROV through splash zone under wave and ship motion. Ocean Engineering. 2021;238.
[53] Sayer P. Hydrodynamic loads during the deployment of ROVs. Ocean Engineering. 2008;35:41-6.
[54] Fang M-C, Hou C-S, Luo J-H. On the motions of the underwater remotely operated vehicle with the umbilical cable effect. Ocean Engineering. 2007;34:1275-89.
[55] Zhao C, Thies P, Lars J, Cowles J. ROV launch and recovery from an unmanned autonomous surface vessel – Hydrodynamic modelling and system integration. Ocean Engineering. 2021;232.